Simulations of the TJNAF FEL with a tapered undulator and experimental results of laser damage

Lampiris, Dimitrios.

Monterey, California. Naval Postgraduate School

NAVAL POSTGRADUATE SCHOOL
Monterey, California

THESIS

SIMULATIONS OF THE TJNAF FEL WITH A TAPERED UNDULATOR AND EXPERIMENTAL RESULTS OF LASER DAMAGE

by

Dimitrios Lampiris

December 2000

Thesis Advisor: William B. Colson
Co-Advisor: Robert L. Armstead

Approved for public release; distribution is unlimited.

REPORT DOCUMENTATION PAGE

Form Approved
OMB No. 0704-0188

1. AGENCY USE ONLY *(Leave blank)*	2. REPORT DATE	3. REPORT TYPE AND DATES COVERED
	December 2000	Master's Thesis

4. TITLE AND SUBTITLE
Simulations of the TJNAF FEL with a Tapered Undulator and Experimental Results of Laser Damage

5. FUNDING NUMBERS

6. AUTHOR
Lampiris, Dimitrios

7. PERFORMING ORGANIZATION NAME(S) AND ADDRESS(ES)
Naval Postgraduate School
Monterey, CA 93943-5000

8. PERFORMING ORGANIZATION REPORT NUMBER

9. SPONSORING / MONITORING AGENCY NAME(S) AND ADDRESS(ES)

10. SPONSORING / MONITORING AGENCY REPORT NUMBER

11. SUPPLEMENTARY NOTES
The views expressed in this thesis are those of the author and do not reflect the official policy or position of the Department of Defense or the U.S. Government.

12a. DISTRIBUTION / AVAILABILITY STATEMENT
Approved for public release; distribution is unlimited.

12b. DISTRIBUTION CODE

13. ABSTRACT

The modern maritime battlefield is dominated by the new generation of sea-skimming, high-speed, stealthy and highly agile anti-ship missiles. Anti-ship cruise missile technology continues to evolve, overcoming the performance of the existing ship self-defense weapon systems. The Free Electron Laser (FEL) could be the ultimate speed-of-light, hard-kill weapon system, offering unique features such as tunability, high power, pinpoint accuracy and infinite magazine. Multimode computer simulations were used to explore the operation of the Thomas Jefferson National Acceleration Facility (TJNAF) FEL with untapered and positively tapered undulator. The final steady-state power, the steady-state gain and the electron energy spread as a function of desynchronism were determined for both 34.5 Mev and 47.5 Mev electron beam energies.

This thesis also includes an experimental study of damage induced to Polyimide Fiberglass and F2 Epoxy samples, by the TJNAF FEL. Irradiations of the samples were conducted changing various parameters such as the wavelength, average power, pulse repetition frequency, cross wind and spot size in order to explore the damage mechanism. At this stage of evolution, TJNAF FEL is capable of 500W output average power, and in order to achieve the required intensity of 10 kW/cm^2 the beam was focused to a small radius. Scaling guidelines were developed in order to predict the damage caused by a high power laser over a large area.

14. SUBJECT TERMS
Free Electron Laser, Ship Self-Defense, Tapered Undulator, Laser Damage Experiments.

15. NUMBER OF PAGES
97

16. PRICE CODE

17. SECURITY CLASSIFICATION OF REPORT	18. SECURITY CLASSIFICATION OF THIS PAGE	19. SECURITY CLASSIFICATION OF ABSTRACT	20. LIMITATION OF ABSTRACT
Unclassified	Unclassified	Unclassified	UL

NSN 7540-01-280-5500

Standard Form 298 (Rev. -89)
Prescribed by ANSI Std. 239-18

THIS PAGE INTENTIONALLY LEFT BLANK

Approved for public release; distribution is unlimited

SIMULATIONS OF THE TJNAF FEL WITH A TAPERED UNDULATOR AND EXPERIMENTAL RESULTS OF LASER DAMAGE

Dimitrios Lampiris
Lieutenant, Hellenic Navy
B.S., Hellenic Naval Academy, 1991

Submitted in partial fulfillment of the
requirements for the degree of

MASTER OF SCIENCE IN APPLIED PHYSICS

from the

NAVAL POSTGRADUATE SCHOOL
December 2000

THIS PAGE INTENTIONALLY LEFT BLANK

ABSTRACT

The modern maritime battlefield is dominated by the new generation of sea-skimming, high-speed, stealthy and highly agile anti-ship missiles. Anti-ship cruise missile technology continues to evolve and to overcome the performance of the existing ship self-defense weapon systems. The Free Electron Laser (FEL) could be the ultimate speed-of-light, hard-kill weapon system, offering unique features such as tunability, high power, pinpoint accuracy and infinite magazine. Multimode computer simulations were used to explore the operation of the Thomas Jefferson National Acceleration Facility (TJNAF) FEL with untapered and positively tapered undulator. The final steady-state power, the steady-state gain and the electron energy spread as a function of desynchronism were determined for both 34.5 Mev and 47.5 Mev electron beam energies.

This thesis also includes an experimental study of damage induced to Polyimide Fiberglass and F2 Epoxy samples, by the TJNAF FEL. Irradiations of the samples were conducted changing various parameters, such as the wavelength, average power, pulse repetition frequency, cross wind and spot size in order to explore the damage mechanism. At this stage of evolution, TJNAF FEL is now capable of 500W output average power. In order to achieve the required

intensity of 10 kW/cm^2 the beam was focused to a small radius, and scaling guidelines were developed in order to predict the damage caused by a high power laser over a large area.

TABLE OF CONTENTS

LIST OF SYMBOLS

A	Spot Area
B	Undulator magnetic field amplitude
c	Speed of light
d	Desynchronism
D	Thermal diffusion length
E_s	Electric optical field amplitude
e	Electron charge
F	Lorentz force
$f(\nu,n)$	Electron spectrum
G	Gain
$G(\nu)$	Gain spectrum
I	Intensity
j	Dimensionless current
$j(z-\tau)$	Longitudial profile of current density
K	Undulator parameter
k	Optical wave number
k_0	Undulator wave number
l_e	Optical Pulse Lengt5h
L	Undulator length
m	Electron mass
N	Number of undulator periods
n	Number of electron passes through the undulator
n_e	Electron density within the electron beam
$N\lambda$	Slippage distance
P	Power
$P(\nu,n)$	Optical power spectrum
Q	Resonator loss factor
r_b	Electron beam radius

S	Resonator length
t	Time
T_r	Atmospheric transmittance
u	Electron speed
$\|\alpha(z, n)\|$	Optical field shape
α	Dimensionless optical field
α_0	Initial dimensionless optical field
B_s	Magnetic optical field amplitude
$\vec{\beta}_z c$	Electron axial velocity component
$\vec{\beta}_\perp c$	Electron transverse velocity component
γ	Lorentz factor
δ	Tapering rate
Δd	Desynchronism range
ε	Absorption coefficient
ζ	Electron phase
η	Efficiency of energy transfer
λ	Optical wavelength
λ_0	Undulator wavelength
μ	Extinction coefficient
ν	Electron phase velocity
ν_0	Initial electron phase velocity
ν_s	Trapped particle oscillation frequency
ρ	Scattering coefficient
σ_z	Dimensionless optical pulse length
τ	dimensionless time
φ	Optical phase

EXECUTIVE SUMMARY

The Free Electron Laser (FEL) could be the solution to the complex problem of ship's self defense against modern anti-ship missiles (ASM). The FEL's immediate response, infinite magazine, speed-of-light target engagement, and continuous tunability make it an excellent alternative of the current Close In Weapon Systems (CIWS).

Computer simulations were used to explore the operation of the Thomas Jefferson National Acceleration Facility (TJNAF FEL) with untapered and positively tapered undulators. Taper rates of $\delta=+4\pi$, $+6\pi$, and $+8\pi$ were used. The final steady-state power, the steady-state gain in weak fields, and the electron energy spread as a function of desynchronism were determined for both 34.5 Mev and 47.5 MeV electron beam energy. The shape of those curves provides useful information about the FEL operation. The final power and gain were significantly smaller for the 47.5 MeV electron beam than for the 34.5 MeV electron beam, because of the lower value of dimensionless current j. However, the general shape of the curves is very similar for each energy. The desynchronism curves present a sharp peak at small values of desynchronism accompanied by the trapped-particle instability. The gain versus desynchronism curves peak at moderate values of d and give near few gain for both small

and large values of desynchronism. Limit cycle behavior was observed in the final power for both the 34.5 MeV and 47.5 MeV electron beams, but not for all tapers. The steady-state power and the steady-state gain turned out to be higher for the conventional undulator than for the tapered undulator. Furthermore, the tapered undulator induces more energy spread to the electron beam, and demonstrates less efficiency for beam recirculation. The width of the desynchronism curve decreased as the tapering rate is increased. The operating width of the desynchronism curves, Δd, as a function of taper has been measured in experiments conducted with the IR Demo FEL at Jefferson Lab [Ref 16]. Simulation results are summarized in Table 1. There is good agreement between theory and experiment.

Electron Beam Energy	**34.5 MeV**				**47.5 MeV**			
Taper- δ	0	4π	6π	8π	0	4π	6π	8π
Maximum Power (dimensionless)	206	141	96	98	170	112	89	9
Maximum Gain (%)	85	58	33	12	76	53	32	12
Desynchronism Curve Width (× Nλ)	0.38	0.3	0.19	0.06	0.34	0.26	0.18	0.04
Limit Cycle Behavior	YES	NO	NO	YES	YES	YES	NO	YES
Maximum Electron Energy Spread (%)	8	8	7.5	7	7	6.5	6	2

Table 1. Summarized Simulation Results.

This thesis also includes an experimental study of damage induced to missile nose-cone materials by the FEL. Experiments were conducted with the TJNAF FEL in order to study the damage caused by the laser beam to some sample materials commonly used in missile cones. The TJNAF FEL is capable at this point of 500 W output power. Since 1 MW power over a spot of 100 cm^2 is approximately required to shoot down a missile, the beam was focused to a small spot area in order to achieve the required intensity of 10 kW/cm^2. In this way several guidelines were developed that could predict the damage caused by a high power laser over a larger area. The pulse repetition frequency (PRF), the wavelength, the average power, the spot size and the crosswind speed were varied during the irradiations in order to determine the influence of these parameters on the damage induced. Airflow of 60-80 mph speed did not have a significant effect, and increased the penetration depth rate by 10%-15%. The penetration depth rate is proportional to the laser intensity. The λ=3.1 μm wavelength was more effective than the λ=4.875 μm wavelength. In addition, the lower PRF (18.7 MHz) seems to contribute to higher penetration rates due to the higher energy per pulse.

THIS PAGE INTENTIONALLY LEFT BLANK

I. INTRODUCTION

In recent years highly sophisticated anti-ship missiles (ASMs) have been introduced to the sea warfare environment making the modern maritime battlefield much more compressed and deadlier than ever before. The ability to react quickly and correctly to multiple ASM attacks is now an essential part of the self-defense capability of a warship. Current ship weapon systems tend to lose their ability to meet this requirement as the offensive missile technology evolves spectacularly. A Free Electron Laser (FEL), as a speed of light, hard-kill weapon system, is a potential solution offering many attractive characteristics in performance, readiness, and life cycle management.

Chapter II of this thesis describes the FEL, and its principles of operation, and gives an overview of background theory. Chapter III addresses the benefits of the FEL as a hard kill weapon system against anti-ship missiles, and analyzes the shortcomings and needs of current ship self defense.

Chapter IV describes the operation of the tapered undulator design, and simulates the performance of the Thomas Jefferson National Acceleration Facility (TJNAF) FEL. Multimode simulations are used to analyze the operation with

untapered and positively tapered undulator, describing the evolution of short optical pulses at far infrared wavelengths. Trapped particle instability and limit cycle behavior are observed and analyzed. Furthermore the steady state power, the steady state gain and the electron energy spread as a function of desynchronism are determined for both 34.5 Mev and 47.5 Mev electron beam energies.

Chapter V presents the analysis of experimental irradiations on several materials commonly used in missile bodies. The goal of the experiments was to determine the amount of damage induced by the unique FEL beam of short pulses and develop scaling laws that could predict the damage caused by a much higher laser power over a large area.

II. FREE ELECTRON LASER THEORY

A. DESCRIPTION AND BASIC OPERATION

The Free Electron Laser (FEL) concept was first introduced by John Madey in 1971. The basic parts of a FEL are the electron accelerator, the undulator, and the optical resonator cavity as shown in Figure 1.

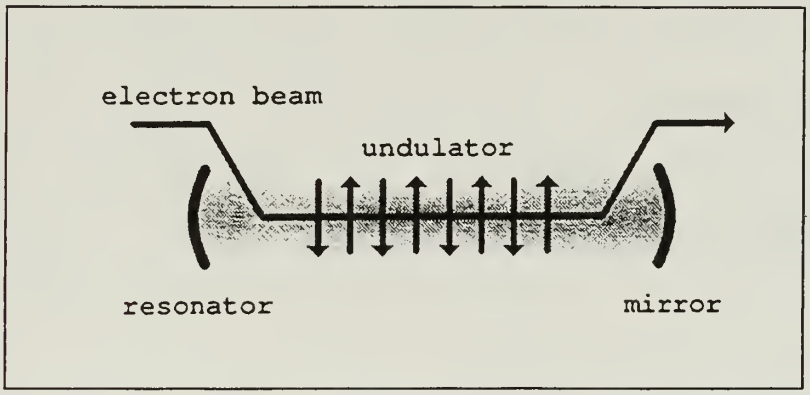

Figure 1. The FEL schematic. (From Ref. 1).

The undulator is a configuration of magnets or superconducting coils, which produce a spatially periodic magnetic field. A relativistic electron beam generated by the accelerator is injected into the undulator. As electrons travel through the undulator, they are periodically deflected in the transverse direction by the imposed magnetic field. This transverse motion causes the electrons to radiate (spontaneous emission) in a narrow forward cone. The electromagnetic radiation is stored in the optical cavity and the optical power grows over many

passes inside the resonator. The coupling of the optical field, the magnetic field, and the electron beam allows extraction of kinetic energy from the relativistic electrons and conversion to high optical power. Subsequent electrons moving inside the undulator interact with the continuously growing optical field and radiate in the presence of light; this is stimulated emission.

The combined effect of the undulator magnetic field and the electromagnetic radiation gives rise to the axial bunching of the electrons at the optical wavelength, allowing them to radiate coherently.

B. PARAMETERS AND TYPICAL VALUES

The FEL's most important operation parameters are listed in Table 2.

PARAMETER	DEFINITION	RANGE
B	Undulator Magnetic Field (rms)	2-7 KG
N	Number of Undulator periods	~ 100
λ_0	Undulator Wavelength	2-10 cm
λ	Optical Wavelength	5nm-5cm
L	Undulator Length	1-20 m
K	Undulator Parameter	0.1-10
γ	Lorentz Factor	5-5000
γmc^2	Electron Beam Energy	MeV-GeV
I	Electron Beam Current	1-1000A
r_b	Electron Beam Radius	1mm-1cm
P_{in}	Input Power	10-100 MW
P_{out}	Output Power	1-10 MW
η	Efficiency of Energy transfer	1%-50%

Table 2. FEL's Operation Parameters.

The undulator parameter K is defined by $K = eB\lambda_0 / 2\pi mc^2$ and its value is usually around 1. The radiation optical wavelength is $\lambda = \lambda_o\left(1 + K^2\right) / 2\gamma^2$ (Ref. 1). The FEL's operating wavelength can be easily tuned simply by adjusting the electron beam energy or the undulator parameter. It is worth noting that the FEL can be designed to work in an extremely wide spectrum of wavelengths and in new wavelength ranges, where there are few powerful sources of radiation like 20μm to 500μm and 20nm to 300nm. This remarkable feature makes the FEL an attractive device, demonstrating its potential for various applications.

C. ELECTRON EVOLUTION INSIDE THE UNDULATOR

1. The Undulator

Two kinds of undulator polarizations are commonly used in FELs, the helical and the planar. The helical undulator consists of superconducting coils and generates a magnetic field $\vec{B} = B\left[\cos(k_0 z), \sin(k_0 z), 0\right]$ on axis with $k_0 = 2\pi / \lambda_0$, and it produces circularly polarized light. The planar undulator consists of an arrangement of magnets and generates a magnetic field $\vec{B} = B\left[0, \sin(k_0 z), 0\right]$ on axis, producing linearly polarized light.

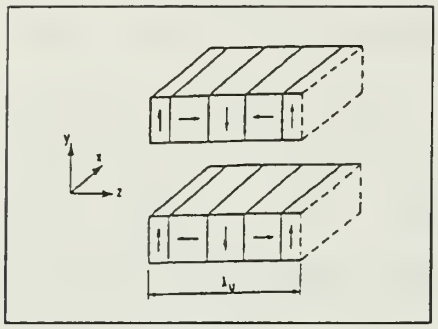

Figure 2. Helical Undulator. (From Ref. 2).

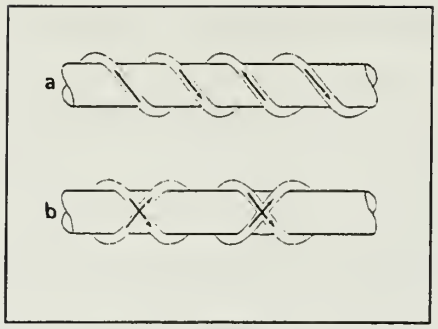

Figure 3. Linear Undulator. (From Ref. 2).

2. Resonance Condition

As electrons move through the undulator in the axial direction, they are periodically deflected in the transverse direction by the spatially varying magnetic field. A typical motion of electrons inside the undulator is shown in the figure below. Note that z and x are the axial and transverse directions respectively.

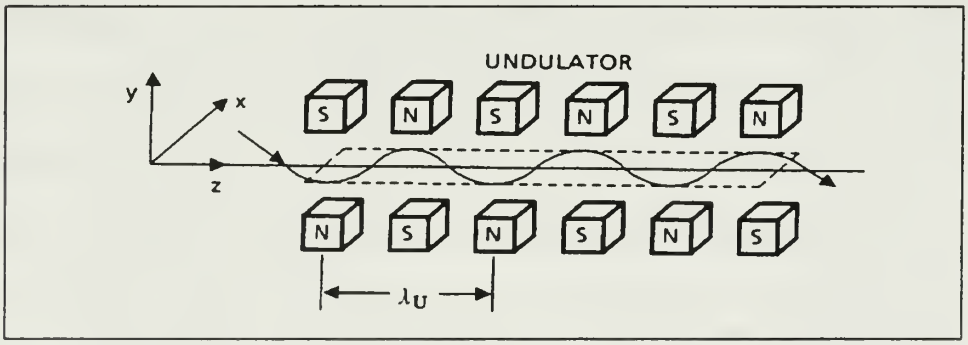

Figure 4. Electron motion inside the Undulator. (From Ref. 2).

As an electron moves through an undulator wavelength λ_0, it completes a full oscillation period in the transverse direction and emits a wavelength of light λ. So one wavelength of light traveling with speed c passes over a slower electron, as it travels through an undulator wavelength λ_0, with speed $\beta_z c$. This particular electron-photon "race" is called the *resonance condition* and is shown schematically in the figure below.

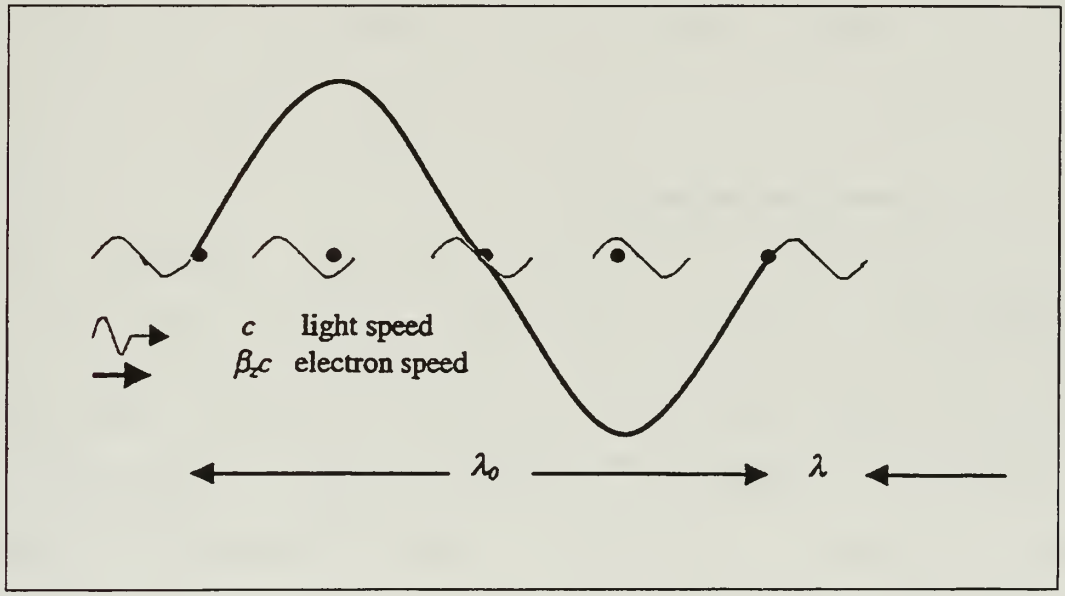

Figure 5. Electron - Photon Race. (After Ref. 3).

The electron acceleration causes the emission of synchrotron radiation in a cone of width $1/\gamma$ (Ref. 2), where $\gamma = 1/\sqrt{1-\beta^2}$ is the Lorentz Factor $\beta = u/c$, and u is the electron's speed.

We define $\beta_z c$ the electron speed in the axial direction, where c is the speed of light. We can easily calculate the wavelength λ of the emitted radiation using the electron-photon speed difference.

$$\lambda = (c - \beta_z c) \cdot \left(\frac{\lambda_0}{\beta_z c}\right) = \frac{\lambda_0}{\beta_z} \cdot (1 - \beta_z) = \lambda_0\left(\frac{1}{\beta_z} - 1\right) \approx \lambda_0 \cdot \left(\frac{1}{1 - \frac{1}{2\gamma^2}} - 1\right) = \frac{\lambda_0}{2\gamma^2 - 1}$$

$$\approx \frac{\lambda_0}{2\gamma^2} \quad \text{and} \quad \beta_z \approx \beta.$$

For highly relativistic electrons, $\gamma >> 1$ and $\lambda \approx \lambda_0 / 2\gamma^2$.

3. Pendulum Equation

We consider a helical undulator magnetic field $\vec{B} = B\left[\cos(k_0 z), \sin(k_0 z), 0\right]$, where $k_0 = 2\pi/\lambda_0$ is the undulator wave number and λ_0 is the undulator wavelength. We assume for the optical field a circularly polarized plane wave, with electric and magnetic fields $\vec{E}_s = E\left[\cos\Psi, -\sin\Psi, 0\right]$ and $\vec{B}_s = E\left[\sin\Psi, \cos\Psi, 0\right]$ respectively where $\Psi = kz - \omega t + \varphi$, φ is the optical phase, $k = 2\pi/\lambda$ is the optical wave number, and λ is the optical wavelength. It should be pointed out that the electric and magnetic fields $\vec{E}_s, \vec{B}_s$ have the same amplitude E, as they are measured in cgs units.

Relativistic electrons with charge magnitude e are injected in the undulator with energy γmc^2 and momentum $\vec{P} = \gamma m\vec{u}$, where γ is the Lorentz factor, m is the electron mass, $\vec{u} = \vec{\beta}c = \vec{\beta}_\perp c + \vec{\beta}_z c$ is the electron's velocity, and $\vec{\beta}_\perp c, \vec{\beta}_z c$ are the velocity components in the transverse and axial direction respectively. Electrons interact with the fields and they experience relativistic force

$$\vec{F} = \frac{d\vec{P}}{dt} = -e\left[\vec{E} + \frac{\vec{u}}{c} \times \vec{B}_T\right]. \qquad [1]$$

$$\text{From [1]} \Rightarrow \frac{d(\gamma\vec{\beta})}{dt} = \frac{-e}{mc}\left[\vec{E} + \vec{\beta} \times \vec{B}_T\right], \qquad [2]$$

where $\vec{B}_T$ is the total magnetic field of the undulator and optical field combined together $\vec{B}_T = \vec{B} + \vec{B}_s$. The magnetic field is always perpendicular to the electron motion and does not affect the electron's energy γmc^2. The electron energy change is given by

$$\frac{d(\gamma mc^2)}{dt} = \vec{F} \cdot \vec{u} = -e\vec{E} \cdot \vec{u} \Rightarrow \frac{d\gamma}{dt} = -\frac{e}{mc}\vec{\beta} \cdot \vec{E}. \qquad [3]$$

Inserting the fields into the Lorentz equation we get

$$\frac{d\gamma\vec{\beta}_\perp)}{dt} = \frac{-e}{mc}\left[E(1-\beta_z)\cdot(\cos\Psi, -\sin\Psi, 0) + \beta_z B\cdot(-\sin(k_0 z), \cos(k_0 z), 0)\right] \qquad [4]$$

$$\frac{d(\gamma\vec{\beta}_z)}{dt} = \frac{-e}{mc}\left[0, 0, E(\beta_x\cos\Psi - \beta_y\sin\Psi) + B\cdot(\beta_x\sin(k_0 z) - \beta_y\cos(k_0 z))\right] \qquad [5]$$

$$\frac{d\gamma}{dt} = -\frac{e}{mc} E\left[\beta_x \cos\Psi - \beta_y \sin\Psi\right]. \qquad [6]$$

For relativistic electrons $E(1-\beta_z) << B\beta_z$, so we can disregard the term $E(1-\beta_z)\cdot(\cos\Psi, -\sin\Psi, 0)$. Within this approximation, integration of equation [4] with respect to time gives the transverse motion as

$$\vec{\beta}_\perp = -\frac{K}{\gamma}\left[\cos(k_0 z), \sin(k_0 z), 0\right] \qquad [7]$$

where K is the undulator parameter and

$$\beta_x = -\frac{K}{\gamma}\cos(k_0 z), \qquad [8]$$

$$\beta_y = -\frac{K}{\gamma}\sin(k_0 z). \qquad [9]$$

We substitute β_x, β_y into equation [6] and obtain

$$\frac{\partial\gamma}{\partial t} = \dot{\gamma} = \frac{eKE}{\gamma mc}\cos(\zeta + \varphi). \qquad [10]$$

The Lorentz Factor γ describes the electron's energy, $\zeta = (k + k_0)z - \omega t$ is the electron's phase generated by the combination of the undulator and optical fields, and ϕ is the optical phase. Since $\lambda << \lambda_0$, $k >> k_0$ and $\gamma >> 1$ (relativistic electrons), the initial electron phase in the beginning of the undulator at t=0 is $\zeta_0 = (k + k_0)z_0 \approx kz_0$.

From equation [7], we have $\vec{\beta}_\perp^2 = \frac{K^2}{\gamma^2}$. Combining this with the Lorentz factor, we get

$$\gamma^{-2} = 1 - \vec{\beta}^2 = 1 - \vec{\beta}_z^2 - \vec{\beta}_\perp^2 = 1 - \vec{\beta}_z^2 - \frac{K^2}{\gamma^2} \approx 1 - \beta_z^2. \qquad [11]$$

Differentiation of [11] with respect to time gives

$$\frac{\dot{\gamma}}{\gamma} = \frac{\gamma^2 \beta_z \dot{\beta}_z}{\left(1 + K^2\right)} \qquad [12]$$

which relates $\dot{\gamma}$ to $\dot{\beta}_z$. Differentiating ζ twice, we acquire

$$\dot{\zeta} = (k + k_0)\dot{z} - \omega = (k + k_0)c\beta_z - \omega \qquad [13]$$

$$\text{and } \ddot{\zeta} = (k + k_0)c\dot{\beta}_z \Rightarrow \dot{\beta}_z = \frac{\ddot{\zeta}}{(k + k_0)c}. \qquad [14]$$

We substitute equation [14] into [12] and get

$$\frac{\dot{\gamma}}{\gamma} = \frac{\gamma^2 \beta_z \ddot{\zeta}}{\left(1 + K^2\right) \cdot (k + k_0)c}. \qquad [15]$$

We now make use of the resonance condition $\lambda = \lambda_o\left(1 + K^2\right)/2\gamma^2$ or $k_0 = k\left(1 + K^2\right)/2\gamma^2$, and assume that for relativistic electrons $\beta_z \cong 1$ and $k + k_0 \cong k$, since $k >> k_0$. Equation [15] becomes

$$\frac{\dot{\gamma}}{\gamma} = \frac{\ddot{\zeta}}{2k_0 c}. \qquad [16]$$

Combining equations [12] and [16], and solving for $\ddot{\zeta}$ we obtain

$$\ddot{\zeta} = \frac{2k_0 eKE}{\gamma^2 m} \cos(\zeta + \varphi), \qquad [17]$$

which describes the dynamics of the electron phase by the **Pendulum Equation.**

The time interval for an average electron to cross the undulator is $\Delta t \cong L / \beta_0 c$, which motivates the introduction of the relevant dimensionless time $\tau = \beta_0 ct / L \cong ct / L$, ranging from 0 to 1 along the whole undulator length L. We use the notation of $\overset{\circ\circ}{\zeta}$ as the second derivative of ζ with respect to τ, and we define $|\alpha| = 4\pi NeKLE / \gamma^2 mc^2$ as the dimensionless optical field amplitude. The pendulum equation takes its final form

$$\overset{\circ\circ}{\zeta} = |\alpha| \cos(\zeta + \varphi). \qquad [18]$$

Certain important remarks must be made from this analysis:

- ζ is a microscopic variable describing the relative position of an electron within an optical wavelength, as it travels through the undulator.
- Equation [10] relates $\dot{\gamma}$, which is the electron's rate of energy change, to the electron's phase $(\zeta + \varphi)$. As $\cos(\zeta + \varphi)$ takes values from -1 to 1 within one optical wavelength, half of electron's

phases result in $\dot{\gamma} > 0$, and the other half give $\dot{\gamma} < 0$, which implies that electrons become spread in energy.

- The fact that $\dot{\gamma} \propto EK / \gamma$ implies that stronger fields result in a larger electron energy change, whereas more energetic electrons (larger γ) reduce the coupling of the undulator and optical fields.
- Electrons becoming spread in energy within an optical wavelength, implies that some of them gain energy and move faster while other lose energy and move slower, thus they become *bunched* on the scale of the optical wavelength.
- Electron motion inside the undulator, which is rather complicated, is described by the well-known *pendulum equation,* which facilitates remarkably the visualization of the electron phase dynamics, and the understanding of the phase space diagrams.

D. DIMENSIONLESS PARAMETERS

Several dimensionless variables can summarize recurring combinations of physical parameters, which govern the FEL operation, and are used to gain insight into the relevant physical processes. An important quantity characterizing many FEL properties is the undulator parameter $K = eB\lambda_0 / 2\pi mc^2$ where B is the rms field strength over each period, λ_0 is the undulator wavelength, and e, m, are the electron charge and mass respectively. In most FELs $K \approx 1$. A pass of the electron pulse through the undulator is described by the dimensionless time $\tau = ct / L$ where $\tau = 0 \rightarrow 1$. The electron phase ζ and phase velocity $\nu = \dot{\zeta} = L[(k + k_0) \cdot \beta_z - k]$, describe the electron velocity and position in a section of the beam one wavelength long, and define bunching and bunching rate of the electrons. The phase and phase velocity are coupled by the dimensionless complex optical field $\alpha = |\alpha| e^{i\varphi}$ through the simple pendulum equation $\ddot{\zeta} = |\alpha| \cos(\zeta + \varphi)$. The field amplitude is $|\alpha| = 4\pi NeKLE / \gamma^2 mc^2$, and determines the electron-bunching rate on the optical wavelength scale. When $\alpha << \pi$ the optical field is weak, and when $\alpha >> \pi$ the FEL operates in the strong field regime. The response of

the optical wave to bunching in the beam is described by the dimensionless current $j = 8N(e\pi KL)^2 n_e / \gamma^3 mc^2$, where n_e is the electron density within the electron beam. The dimensionless current provides the coupling between the electron beam and the light wave through the wave equation $\dot{\alpha} = -j\langle e^{-i\zeta} \rangle$ (Ref. 1). When $j<<\pi$ the FEL gain is low, and when $j>>\pi$ the FEL gain is high. Each definition above, ζ and ν describing the electrons, α describing the light wave, and j describing the whole FEL, is physically meaningful and useful in evaluation of many FEL effects.

E. GAIN SPECTUM

Figure 6 shows the FEL gain spectrum for a typical low current FEL with j=2 and N=21, as the initial optical field amplitude α_0 evolves from 0 to 40. G is the FEL gain for one pass of the electron beam through the undulator in a single optical mode, and ν_0 is the initial electron phase velocity at the beginning of the undulator. Figures 7, 8 and 9 present a cross section of the gain spectrum for $\alpha_0 = 0$, $\alpha_0 = 20$ and $\alpha_0 = 40$ respectively. The plots were generated by computer simulations. The gain has a maximum value (peak gain), for each optical field strength α_0. Furthermore, the position of the peak gain changes as α_0 increases, and the gain spectrum distorts.

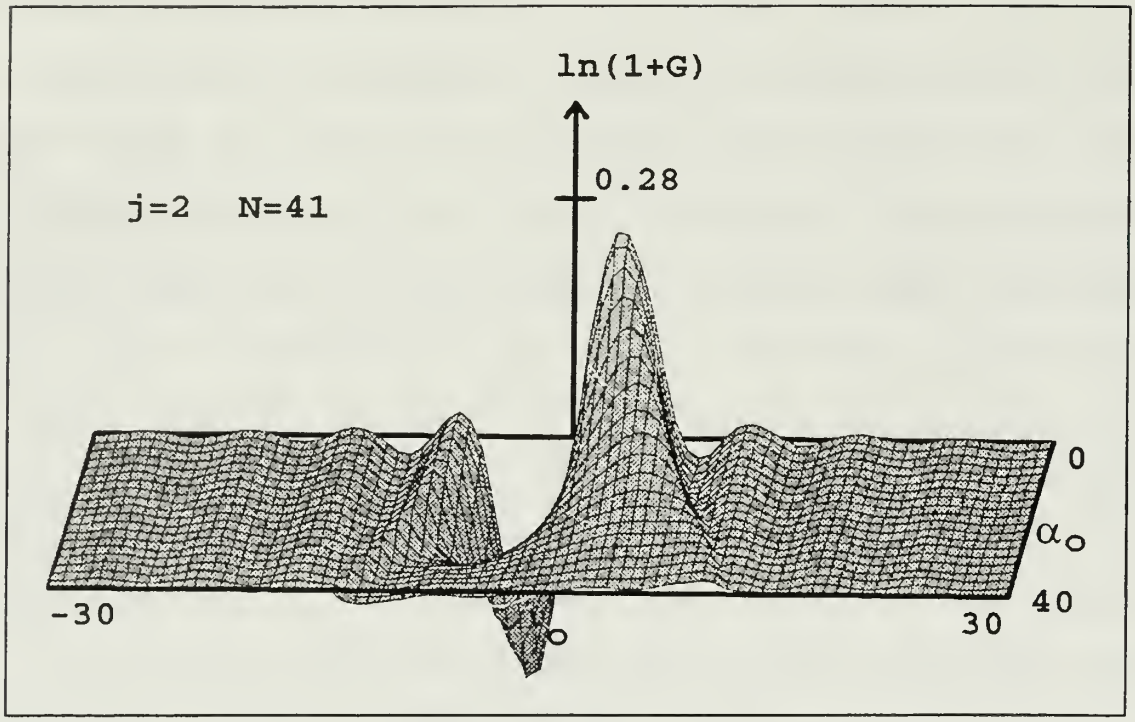

Figure 6. FEL Gain Spectrum, j=2.

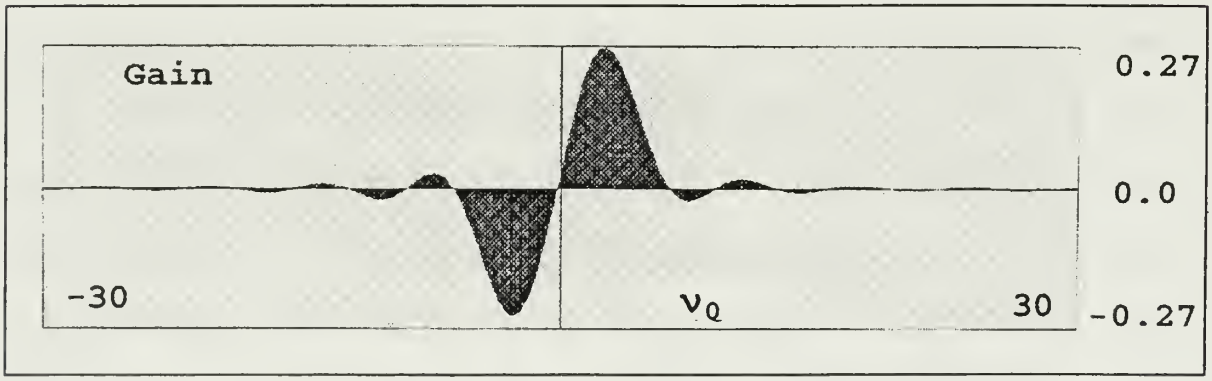

Figure 7. FEL Gain Spectrum, j=2, $\alpha_0 = 0$.

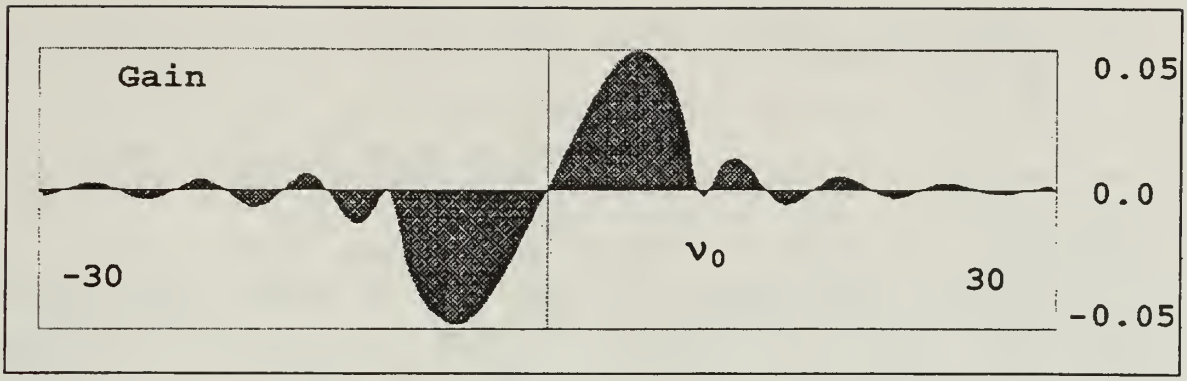

Figure 8. FEL Gain Spectrum, j=2, $\alpha_0 = 20$.

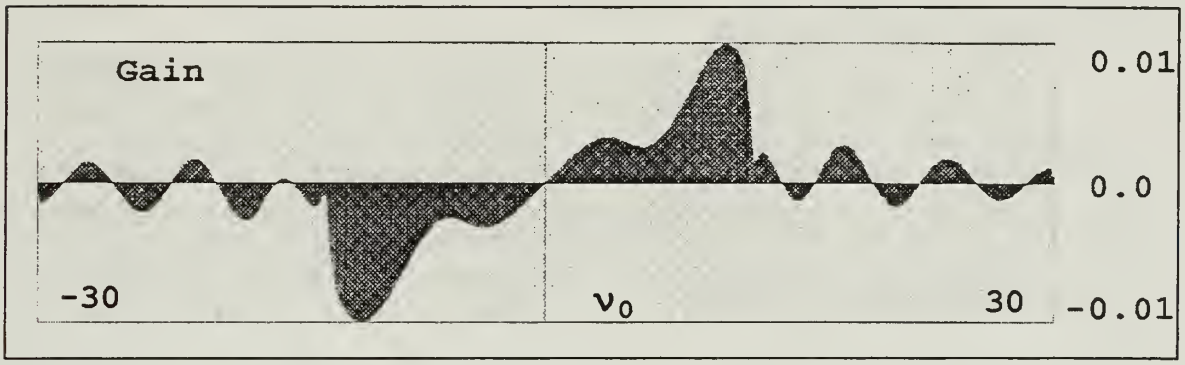

Figure 9. FEL Gain Spectrum, j=2, $\alpha_0 = 40$.

The value and the position of the peak gain are crucial to the FEL operation, since they determine the optical frequencies that are going to be amplified as well as the final optical power. The FEL gain is clearly antisymetric about resonance $\nu_o=0$. In weak optical fields the gain spectrum has a peak value of $G \approx 0.13j$ at $\nu_o = 2.6$, and width $\Delta\nu_o \approx \pi$. The gain is zero at resonance. As the optical field grows to saturation the gain spectrum distorts, and becomes broader with width $\Delta\nu_o \approx \sqrt{\alpha}$. The peak

gain decreases substantially and moves to higher values of ν_o. In the case of j = 2, the peak gain drops from 27% in weak optical fields, to 1% when the optical field saturates. The phase velocity of peak gain moves from $\nu_o = 2.6$ to $\nu_o = 10.8$. The corresponding change in the wavelength is $\Delta\lambda/\lambda = \Delta\nu_o/4\pi N = 3\%$ in this example.

F. FEL'S APPLICATIONS

The FEL mechanism can be designed to operate over a large region of wavelengths, from nanometers to centimeters. Each FEL also has the capability of being continuously tuned simply by changing the electron beam energy. Most often the FEL is operated so that the net energy transfer is from the electron beam to the radiation field in order to amplify it. Nevertheless, it is possible to operate the FEL so that the net energy transfer is from the radiation field to the electrons making an accelerator or an inverse FEL.

The FEL has become an exciting alternative to other radiation sources, like microwave tubes and lasers, and can extend the operational range of both. Because of its flexibility, the FEL can be applied in many diverse areas such as lithography, plasma heating, particle acceleration, as well as material, biological, medical, and solid state research.

III. THE FEL AS SHIP SELF- DEFENSE WEAPON

A. THE ANTI-SHIP MISSILE THREAT

In the modern naval battlefield, anti-ship missiles (ASM) have become a very serious threat even to the most modern and complex warships. Faster and faster ASMs have dramatically decreased response times for surface vessels. A simple scenario helps us realize the complexity of the problem.

Consider a sea skimming ASM, flying less than 10 meters above sea level and heading towards a ship. Let the height of the ship's sensors be 25 meters above the sea surface, so that the horizon distance in which the missile can be detected and tracked is approximately 10 nautical miles (nm). Given the missile's speed to be 1 mach = 600 knots = 10 nm/min, it takes one minute for the missile to impact the ship. The time is decreased to 30 seconds if the missile approaches with speed mach 2.

The Aegean Sea, where the Hellenic naval combatants usually operate, has a very specific geography. It is a complex of thousands of neighboring islands, less than 12 nautical miles apart each other. This complicated battle arena gives rise to certain specific scenarios. For instance, a battleship operating 5 nautical miles from the

coast of a small island could suddenly be face to face with a Harpoon ASM emerging behind the island, using the waypoint navigation feature.

Due to the spectacular development of anti-ship missile technology, ASMs have become state-of-the art weapons with highly supersonic speeds, ten's of g's maneuverability, multiple guidance modes, countermeasure capability, reduced radar cross section and IR signature, and pinpoint accuracy. There seem to be no end to this development making it hard for the ship self-defense systems to keep pace.

B. SHIP SELF-DEFENSE

The existing shipboard anti-missile systems are divided into two major categories: passive and active. Passive methods include decoys, chaffs, stealth technology, as well as tactics and techniques, which alter the ship's IR or RADAR signature, and generally deceive and confuse the missile sensors.

On the other hand, active systems imply strong interaction with the incoming missile target and they are further divided into two categories: soft kill and hard kill. Soft kill methods disable the threat missile by attacking its electronics or blinding its sensor, but

otherwise leaving the target body undamaged. Hard kill weapon systems actually destroy the target-missile achieving large-scale physical damage. We are going to be focused on the hard kill method, which is the most desirable. A scenario of layered ship self-defense, involving both soft kill and hard kill methods, is demonstrated in Figure 10.

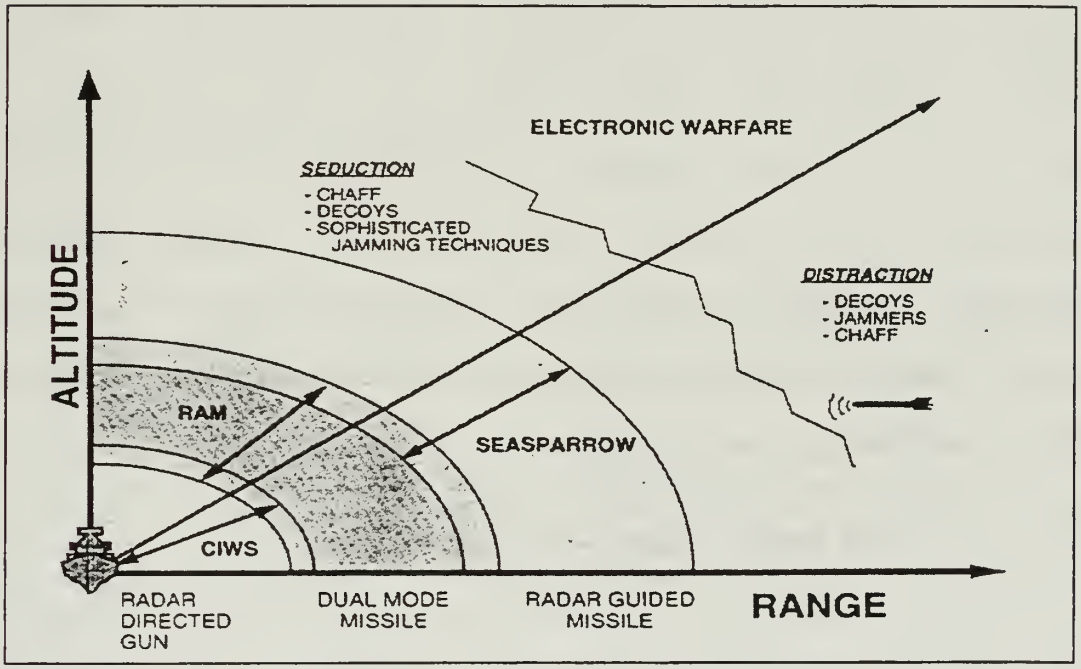

Figure 10. Layered Ship Self-defense. (From Ref. 10).

C. AVAILABLE HARD KILL WEAPON SYSTEMS

Several hard kill weapon systems are used to confront the complicated ASM threat.

1. Large Caliber Guns

The 5/54 or 3/62 OTOMELARA guns have effective ranges of 10 and 5 nautical miles respectively, and are the standard Hellenic Navy guns that can be used as a medium range defense, but with extremely low efficiency. The fire control system, the shell's speed, and the relatively slow rate of fire are not capable of shooting down an approaching supersonic sea skimming ASM with high maneuverability. Moreover, the shell dispersion (increasing with large range) limits the accuracy considerably and lowers the probability kill to minimal values.

2. Long Range Surface-Air Missiles

Another approach considered as a long-range defense is the use of antimissile missiles. Several surface-to-air missiles, such as the standard Navy missile (SM-1, SM-2) or the Nato Sea Sparrow (NSSM) have been developed, and are equipped with excellent flight characteristics, maneuverability, and effective range.

However, in order to take advantage of the long effective range, a long detection range is also required.

Since the sea skimming ASM missile's flight altitude is about 8 m with a corresponding detection range at the horizon of 11 nautical miles, making the long-range missile advantage becomes useless. Moreover, physical dynamics require that defensive missiles should have 2 to 3 times the maneuverability of the incoming missile. Current anti-ship missiles have the ability to fly at supersonic speeds, pulling more than 10g in terminal maneuvers. A simple calculation makes the maneuvering requirements of the defensive missile unfeasible.

3. CIWS

The innermost layer of defense against anti-ship missiles is provided by the Close In Weapon Systems (CIWS). The inner layer defense systems could be gun based, such as Raytheon's 20mm Phalanx, FABA's 20mm Meroka, Signaal's 30mm Goalkeeper, Oerlicon - Royal Ordance 35mm Millenium, or OTOBreda's twin 25mm Myriad. Some Navies advocate short-range missile based CIWS's such as the US-German RAM or the French Mistral. The basic characteristics and features of the currently most used CIWS are discussed below.

a) The Phalanx Gun

At this time, the Phalanx Gun is the standard CIWS for both the U.S and Hellenic Navies. It is the most extensively used CIWS in the world with more than 700 Phalanx systems deployed by 21 Navies. Since 1979, when it was initially deployed, the weapon has evolved from Block 0 to Block 1B through system improvements, upgrades, and modifications. The system is a rapid fire, computer controlled radar and gun system that automatically carries out search, detection, target threat evaluation, tracking, and firing. It is equipped with an electronically controlled, pneumatically driven, 20 mm six-barrel gun capable of firing 4500 rounds per minute within a range of 2 km. Although the weapon provides superior performance against anti-ship missiles, it has several deficiencies. It experiences random and variable bullet dispersion, which diminishes its ability to destroy its intended targets at a range where missile debris does not hit the ship. The high rate of fire causes overheating of the barrels, so that the firing must be limited to bursts of only few seconds. The gun's magazine, which is capable of holding up to 1000 rounds, can be expended in just four to five engagements and requires up to 30 minutes to be reloaded. If the missile attacks are more frequent, it means that the ship is left

with no self-defense. Finally, computer simulations have shown that the probability of hitting an incoming missile is extremely low for ranges more than 250 m (Ref. 11). In Figure 11 we can see the probability of a single phalanx gun penetrator hitting an incoming missile flying at altitude of 7 meters above sea surface with speed Mach 2, versus the missile range from the ship. It is easy to see that the probability drops very rapidly as the range increases.

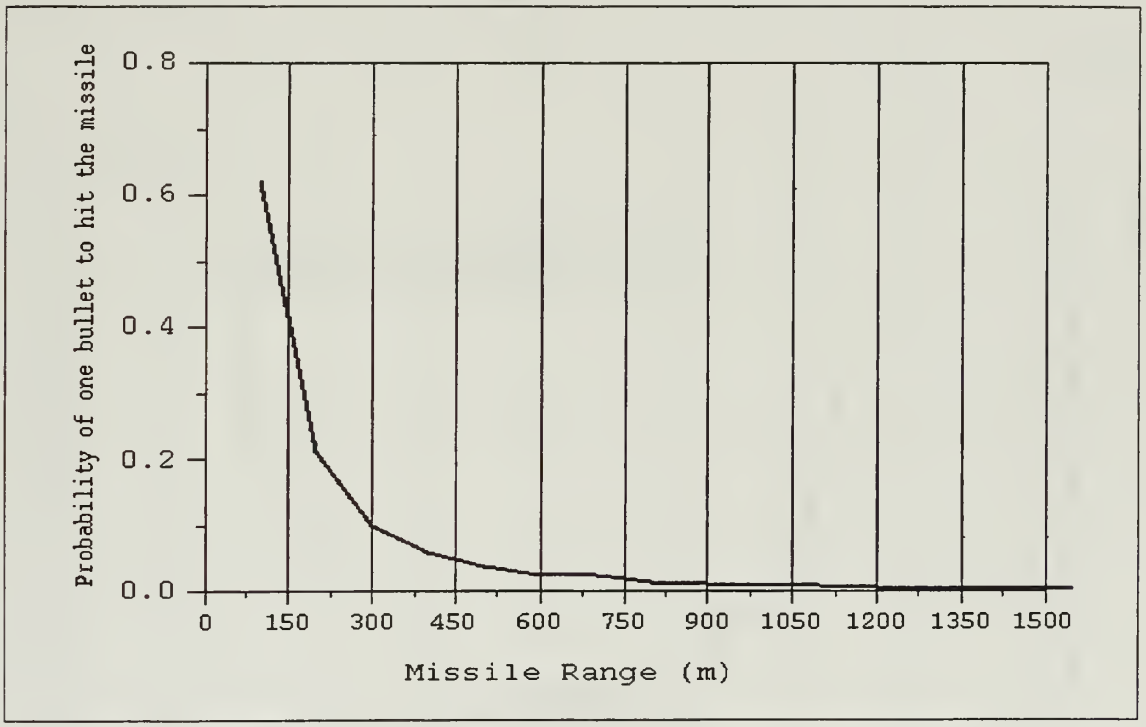

Figure 11. Probability of a single round to hit the missile versus missile range.

Figure 12, shows how the number of hits acquired by a missile with approach speed Mach 2 and altitude 7 m above the sea level, varies with range from the ship. The dashed line is for a firing rate of 3000 rounds/min (Block 1A model), while the solid line is for 4500 rounds/min (Block 1B model). Since 5 to 6 hits are needed to destroy the missile a typical killing range seems to be around 150 m from the ship. The missile may be destroyed within a range of 100 to 200 m, but its fragments contain enough kinetic energy to reach the ship and cause serious damage.

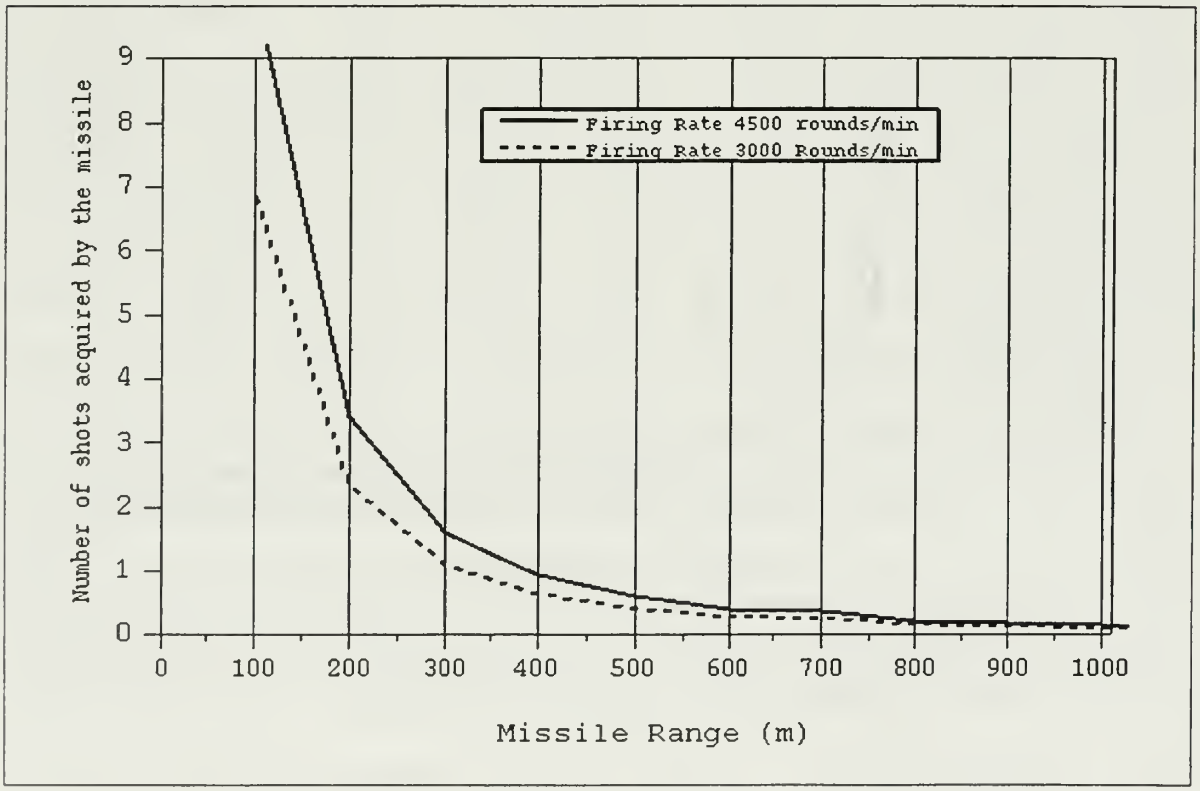

Figure 12. Number of shots acquired by the missile versus range.

Figure 13 presents the probability of a missile fragment hitting the ship versus the missile destruction range. It is clear that the probability increases dramatically when the missile is destroyed closer to the ship. For a missile, approaching with Mach 2 speed and 7 m altitude destroyed by the Phalanx Gun at 200 m from the ship and breaking into 20 pieces, there will be about 10 of them that finally hit the ship.

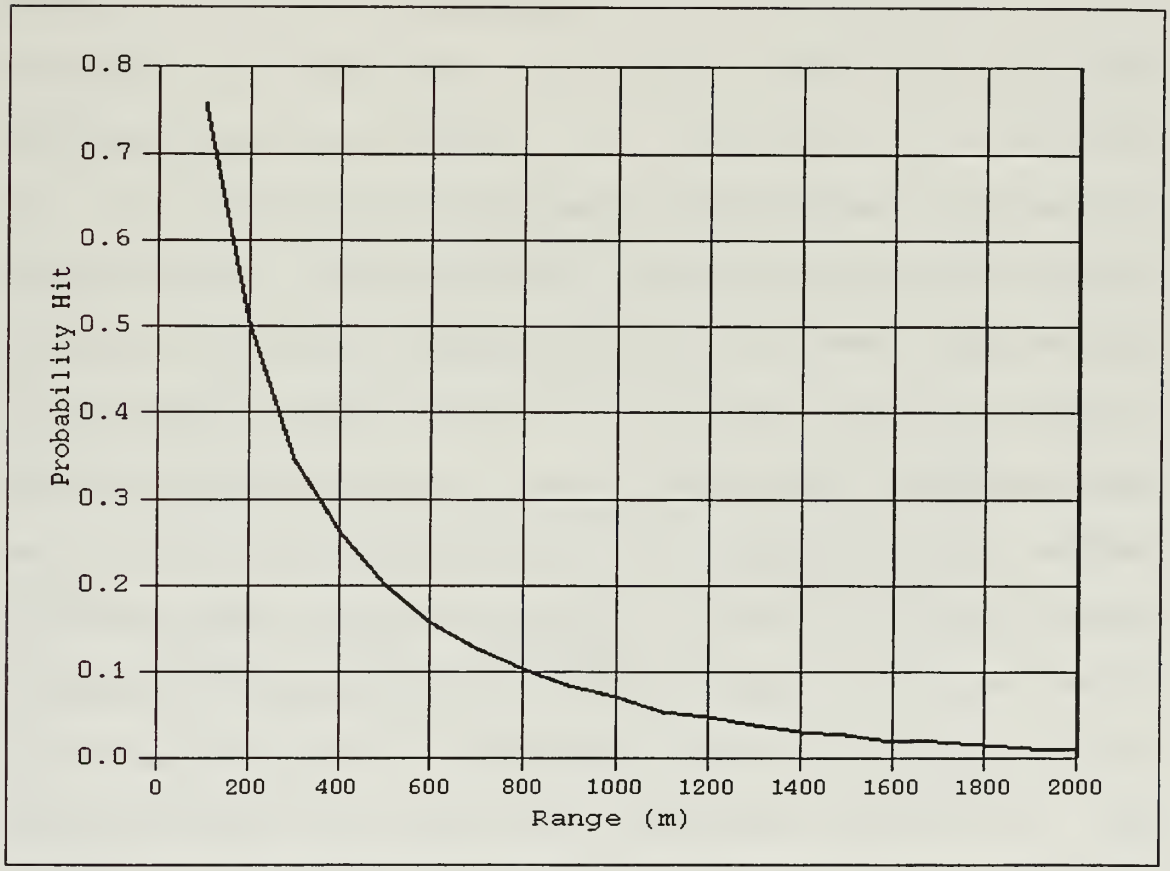

Figure 13. Probability of a single missile fragment to hit the ship versus the missile destruction range.

b) The Rolling Airframe Missile (RAM)

Another relatively new weapon system is the American/German Rolling Airframe missile (RAM) that was first introduced in 1993 to counter the anti-ship cruise missile threat. It is a lightweight quick reaction, high firepower guided missile weapon system that provides another layer of hard kill defense and fills the gap between the Phalanx CIWS and the longer-range anti-missile missile system as the Nato Sea Sparrow.

RAM comes with a 21-round guided missile launcher, which provides high firepower. The supersonic missile demonstrates an excellent kill performance resulting from its high maneuverability and accuracy as well as from its effective warhead and fusing. Moreover, the latest missile upgrade RAM Block 1 Infrared (IRMV) exhibits multiple guidance modes, reduced IR and Radar signatures, countermeasures capability, and improved performance in degraded weather conditions such as heavy rain or fog. The currently produced RAM missile (Block 0) has been fired in 105 flight tests resulting in 100 successful intercepts. Its reliability has been sustained in extensive field tests under high stress conditions and realistic scenarios thus demonstrating that RAM is one of the world's most advanced ship self-defense weapon systems. Another system that is also under development is the Raytheon's SEA RAM, which

combines elements from both Phalanx and RAM CIWS. An 11-missile round RAM launcher assembly loaded with RAM B1 guided missiles replaces Phalanx's 20mm gun. SEA RAM inherits RAM's accuracy, extended range and maneuverability combined with the Phalanx's Block 1B's high resolution target detection search and track sensor systems and reliable quick-response capability. SEA RAM is an affordable capability upgrade and especially attractive option for those navies that have already deployed the Phalanx, like the Hellenic Navy. It fits the exact footprint of the Phalanx, uses the same power and requires a minimal ship modification.

Nevertheless, anti-ship missile technology evolves extremely fast, ASMs have not yet reached the peak of their evolution. Future high performance threats are expected to be stealthier, faster, and lower flying missiles able to perform unique maneuvering profiles in order to defeat ship defenses. Since a defensive missile is required to have substantially superior speed, guidance system, and maneuverability than the incoming threat, it is a matter of time that RAM or any current missile based inner layer defense system will become outdated and ineffective. The defensive - offensive missile technology race is clearly won by the offensive one.

D. DEFENSE AT THE SPEED OF LIGHT

So far, only kinetic kill methods have been used to project power to the target, generally in the form of projectiles, rockets and missiles. Kinetic energy weapons require a finite flight time to intercept a target. This time turns out to be crucial when a threat is approaching with supersonic speed, making the reaction time for the ship minimum and leaving no chance for reengagement.

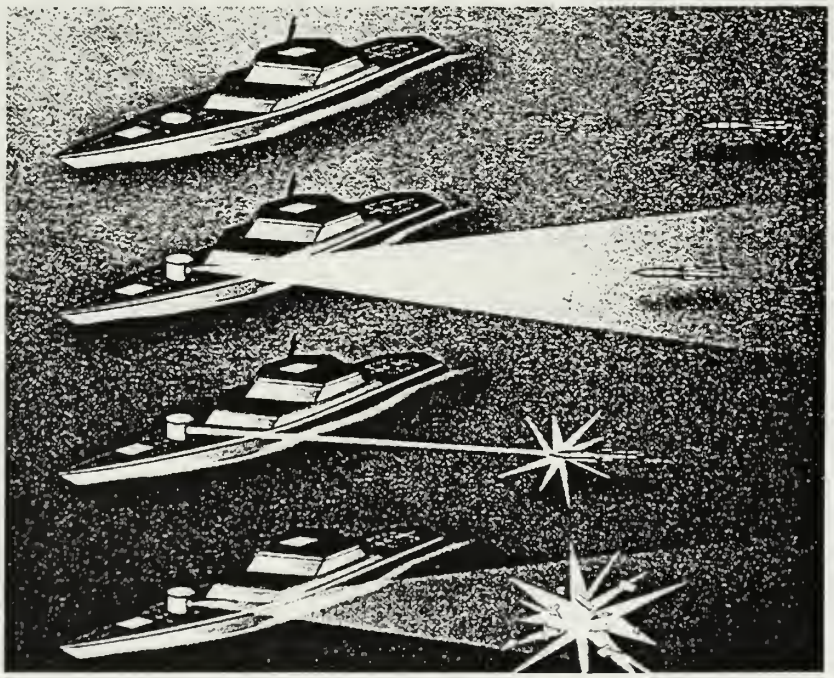

Figure 14. HEL Engagement Scenario. (From Ref. 7).

High Energy Lasers (HELs) are now being developed to be used as weapons delivering lethal power at the speed of light. A high power optical beam traveling with the amazing speed of 300,000 km/sec is now available to boost ship's self-defense. The HEL provides an effective engagement range of approximately 10 km and a practically zero flight time out to the target. In the case of a typical short-range (10 km) engagement with a modern defensive missile system, the time between the employment and threat destruction can be as big as 10 seconds. In the unfortunate case of a miss there is no time for reengagement. On the other hand it takes only 30 μsec for the laser beam to reach the target and about 2 seconds to destroy it. Such a short time provides the benefit of a "second chance", if there is a miss and moreover the advantage of engaging multiple threats.

An example of an HEL is MIRACL (Mid-Infra-Red Advanced Chemical Laser), which has been developed at White Sands Missile Range in New Mexico. MIRACL is a deuterium fluoride laser that operates at 3.8 μm wavelength, and has achieved an output power of 2.2 MW. At tests conducted in February of 1996 under the Nautilus program, MIRACL successfully engaged and destroyed a short-range rocket in flight using the Sea Lite pointing and tracking system.

Undoubtedly, the HEL could enhance substantially a ship's self-defense capability, and HEL development should be considered seriously to provide an alternative to current short-range defense weapons. It is the weapon of the 21st century and will always be effective. Its instantaneous response and amazing capabilities can never be outdated, as the speed of light will never be exceeded by the performance of any future advanced missile.

E. LASER BEAM LETHALITY

The HEL weapon concept is fundamentally different from that of the kinetic energy weapon. A kinetic energy weapon requires a finite time to deliver its warhead or mass to the target, but causes damage instantly. On the other hand, the laser beam arrives at the target instantly, but it takes a finite time to cause damage. The damaging effect of the HEL is a thermal process nearly identical to cutting a peace of metal with a blowtorch. The question posed is how lethal a laser beam has to be in order to shoot down a flying missile.

Although it is preferable, it is not necessary to cause the ignition of the warhead in order to destroy a flying target. A hole of the dimensions of a child's fist (3cm x 3cm x 3cm) is generally enough to cause severe damage to the

missile's electronics. Furthermore, this damage significantly alters the missile's aerodynamics resulting to instability, overheating and fall. The power required to make such a hole depends on the missile's material. As a rule of thumb, we can say that it takes a few electron-volts (eV) energy to break a chemical bond, and separate atoms. A typical 1 liter chunk of material to be removed from the missile consists of about 10^{25} atoms, so that about 3 MJ energy is needed to create such a hole. Limiting the delivering time of this energy to 2 to 3 seconds, the needed power should be about 1 MW. After considering diffraction, the laser beam is focused at the target in an area of $100 cm^2$ so that the intensity is about 10 kW/cm^2. In order to get a feeling of the magnitude of this intensity, we can mention that 35 W/cm^2 on the human body results in third degree burns with destruction of the dermis and epidermis. It must be noted that delivering time cannot be diminished without a limit. Smaller delivery times, which imply very high power, may cause detrimental, nonlinear effects such as thermal blooming. These effects form a lens in the atmosphere and spread the laser beam diminishing the power at the target dramatically. Thermal blooming will be discussed in the following section.

F. PROPAGATION OF THE LASER BEAM THROUGH THE ATMOSPHERE

1. Transmittance

The atmospheric components (elements and compounds) strongly affect the propagation of the Laser beam and can dramatically diminish the required optical intensity at the target. There are three primary processes that affect the transmission of radiation through the atmosphere: absorption, scattering, and random refractive index fluctuations (turbulence).

Absorption is a quantum process where an atmospheric molecule absorbs the energy from some incident photon and occurs when certain types of particles interact with the propagating electromagnetic radiation. Water, vapor, carbon dioxide, ozone, nitrous oxide, and carbon monoxide are the major radiation absorbers. Scattering is the redirection of radiation by particles in the air. Photons collide with these particles, whereas the photon energy is reradiated in all directions. Turbulence describes the time-space varying temperature and pressure inhomogenuites, which result in considerable index of refraction fluctuations. The index of refraction variations cause the direction of light propagation to bend in various directions.

Absorption and scattering are grouped together under the topic of extinction. Extinction is defined as the attenuation in the amount of radiation passing through the atmosphere. Absorption and scattering are described respectively by the absorption coefficient ε and scattering coefficient ρ, while extinction is described by the extinction coefficient $\mu = \varepsilon + \rho$ [km]. Transmittance (Tr) through the atmosphere over a distance x is defined as $Tr = e^{-\mu \cdot x}$, and the irradiance at a target at distance x is $I(x) = I_0 e^{-\mu \cdot x} = I_0 Tr$. Both ε and ρ, and therefore the transmittance Tr, strongly depend on the radiation wavelength.

The atmospheric transmittance over a wavelength range is extremely crucial to directed energy because it determines the choice of the suitable propagating wavelength. Transmittance depends on the composition, density and pressure of the atmospheric components together with the optical line strengths and line widths of all the spectroscopic transitions of the molecules and the number, size and composition distributions of the particles.

This complex problem has been described by computer modeling codes such as LOWTRAN, FASCODE and MODRAN. MODRAN and FASCODE are currently the most widely used and have the

capability to handle arbitrary geometries and view conditions, while they allow the user to select from several model atmospheres, aerosol profiles, and other weather conditions. A graph of a typical atmospheric transmission in a maritime aerosol model is shown in Figure 15. Note the strong dependence of the transmittance on optical wavelength. There are specific windows of high transmittance where it would be preferable to operate a laser. To achieve a wavelength in one of these windows, a laser must be tunable. This feature is unique to an FEL; other lasers are confined to specific wavelengths.

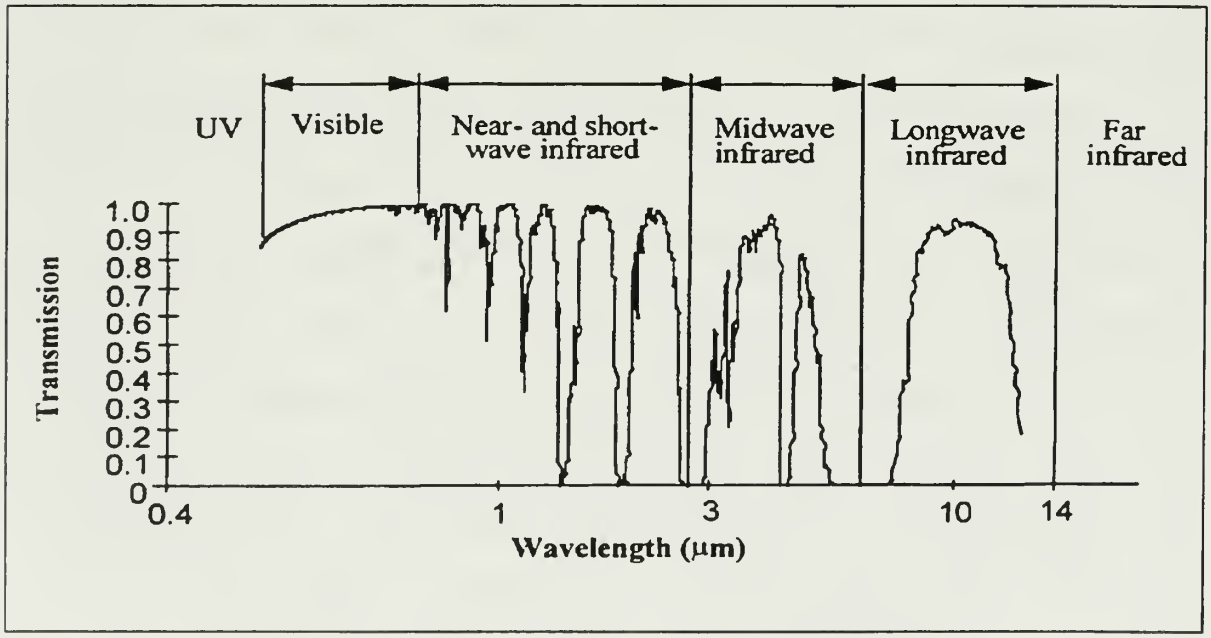

Figure 15. Atmospheric Transmittance. (From Ref. 5).

2. Nonlinear Effects

A high power optical beam traveling through the atmosphere is also subject to a "nonlinear" effect where the propagation medium is modified by the radiation. This nonlinear effect is called thermal blooming, and takes place when the absorption of the beam energy by the atmosphere causes a local temperature rise followed by a density change. Since the refractive index depends on the atmosphere density, a local refractive index gradient across the laser beam cross-section forms a lens along the beam path. This effect can result in spreading, distortion, and bending of the laser beam, while it generally reduces the power density at the target. In fact, it can limit the irradiance to a value independent of the transmitted power. Nonlinear effects depend on wavelength, pulse length, intensity, and such medium properties as composition and density.

As a result, it is not possible to increase the laser power without limit, and continue to have the laser beam propagate through the atmosphere. Nonlinear effects can lead to dispersion of the beam power, and even complete blockage.

G. THE FREE ELECTRON LASER (FEL)

Among the various types of existing lasers, the FEL turns out to be an excellent candidate for a ship self-defense weapon system. It can be easily integrated in the ship's structure and become a major weapon system. The electrical power required for the FEL's operation can be provided by the ship's power system or by large capacitors. The weight and volume of all the FEL components together are approximately 150 tons and 140 m^3 respectively [Ref. 8], and can be accommodated in a ship the size of a frigate or a destroyer.

The FEL offers significant advantages over other types of lasers. The continuous tunability over a wide range of wavelengths allows the opportunity to select the frequency that best propagates through the atmosphere. FELs do not produce hazardous and toxic wastes, which can be life threatening for the ship's crew as do chemical lasers. Finally the FEL shows the possibility of high wall plug efficiency (~10%), making good use of the ship's valuable power resources. The fact that it operates with electrical power, equips the FEL with an infinite magazine, enabling it to minimize reaction time and engage multiple targets.

IV. SIMULATION RESULTS

A. THE TAPERED UNDULATOR

At normal saturation, the electrons lose enough energy to drop out of the gain spectrum bandwidth. At resonance we have $\nu = 0$ and $\lambda = \lambda_0(1 + K)^2 / 2\gamma^2$ and is only near resonance that the coupling between the electron beam and the light wave is significant. If λ_0 or K are decreased as γ decreases, as electrons lose energy, resonance would be restored, and the interaction could continue to higher optical powers. Increasing λ_0 or K also extends the FEL saturation limit. Decreasing or increasing, tapering or inverse tapering, the undulator wavelength λ_0 or K along z, modifies the simple pendulum equation to include an additional torque, or phase acceleration δ, so that $\overset{\circ}{\nu} = \overset{\circ\circ}{\zeta} = \delta + |\alpha| \cos(\zeta + \varphi)$. If $\delta>0$, we have the case of the "tapered" undulator, while for $\delta<0$, the undulator is "inverse tapered". The value of δ is given by $\delta = -2\pi N \Delta\lambda_0 / \lambda_0$ when the undulator wavelength is decreased, or by $\delta = -4\pi N K^2 \Delta B / B\left(1 + K^2\right)$ when the undulator field strength is decreased.

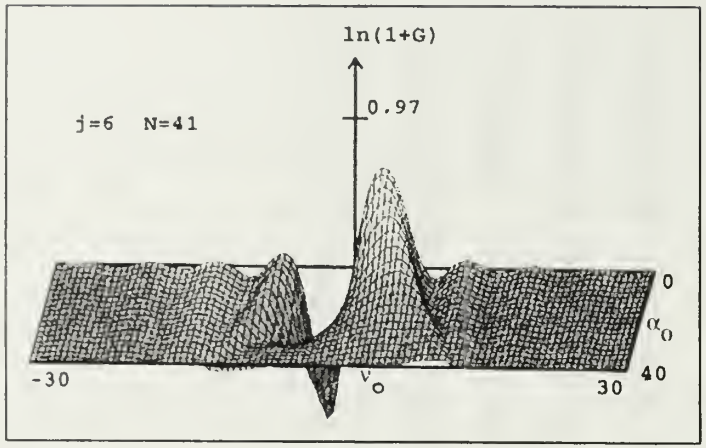

Figure 16. Untapered Undulator.

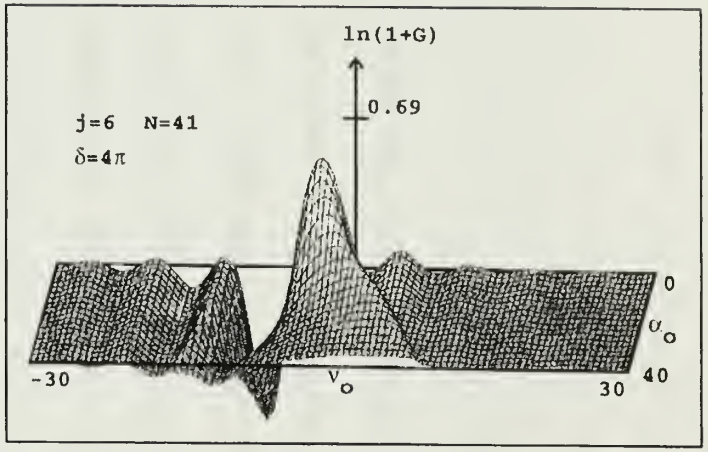

Figure 17. Tapered Undulator, δ=4π.

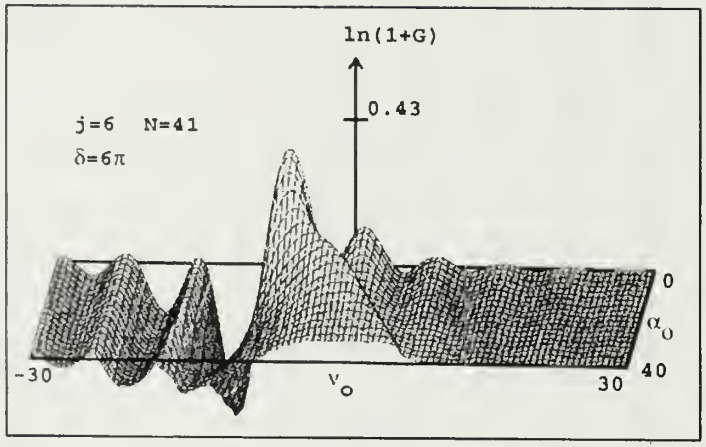

Figure 18. Tapered Undulator, δ=6π.

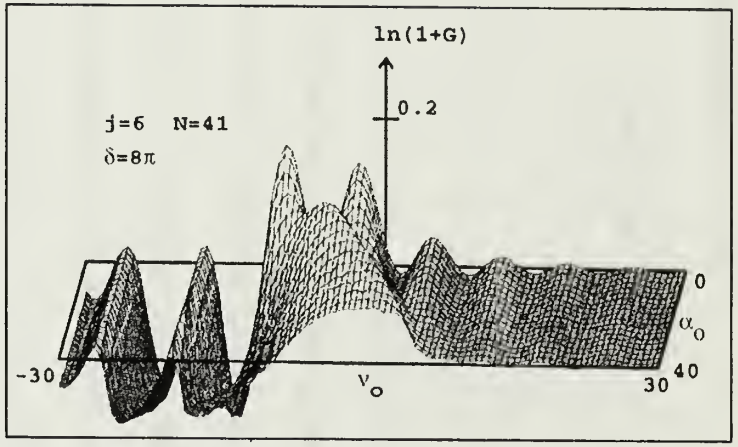

Figure 19. Tapered Undulator, δ=8π.

Figures 16-19 show the computer-simulated gain spectrum, as in Figure 6, of an FEL with dimensionless current j=6 and N=41 periods, for various tapering rates δ. We can see that as the tapering rate δ increases, the gain spectrum is no longer antisymmetric about resonance, but distorts as the bandwidth broadens. The gain in weak optical fields ($\alpha_0 \ll \pi$) is bigger in the untapered case, while in the strong field regime the gain is increased because of taper. Figure 20 presents the peak gain of an FEL with j=6 as a function of taper, for three different optical field strengths α_0. In weak optical fields, $\alpha_0 \approx 0$ when the magnitude of δ increases, the peak gain decreases. The peak gain curve is symmetric in δ with peak value at δ=0. When the optical field becomes stronger, the shape of the curve is distorted; the peak value decreases and shifts to negative values of δ. Figure 20 shows how the tapered undulators have higher gain in strong optical fields than the untapered case, δ=0. In strong optical fields $\alpha_0 = 40$ with j=6, the maximum gain is 9% achieved with $\delta=-4\pi$. For δ=0, the maximum gain in strong fields is only 4%. For positive values of δ and $\alpha_0 = 40$, the maximum gain of 8% is achieved with $\delta=10\pi$.

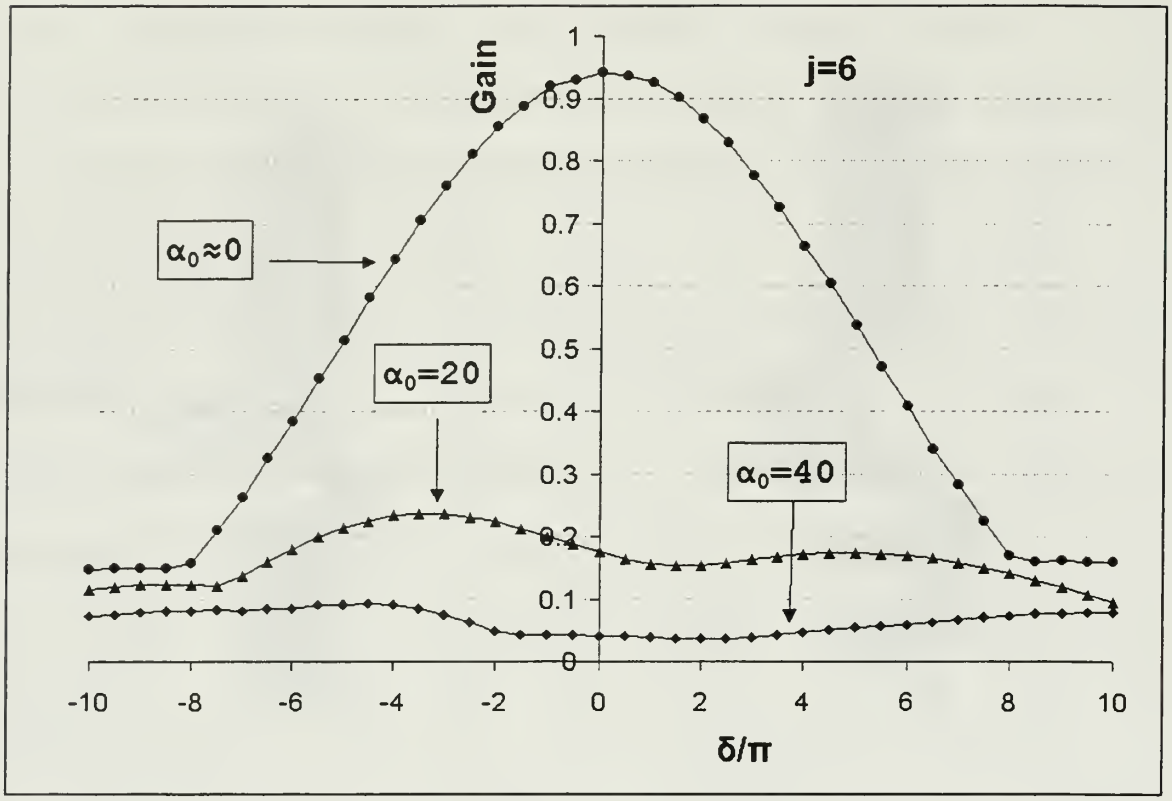

Figure 20. Plot of peak gain versus tapering rate.

Figure 21 presents a plot of the value of phase velocity $\hat{\nu}_0$ giving peak gain in weak fields as a function of the tapering rate δ. In weak fields and for moderate taper rate ($0<\delta<10\pi$), the gain peaks at phase velocity $\hat{\nu}_0 = 2.4 - \delta/2$. Larger taper rates and strong fields alter this relation.

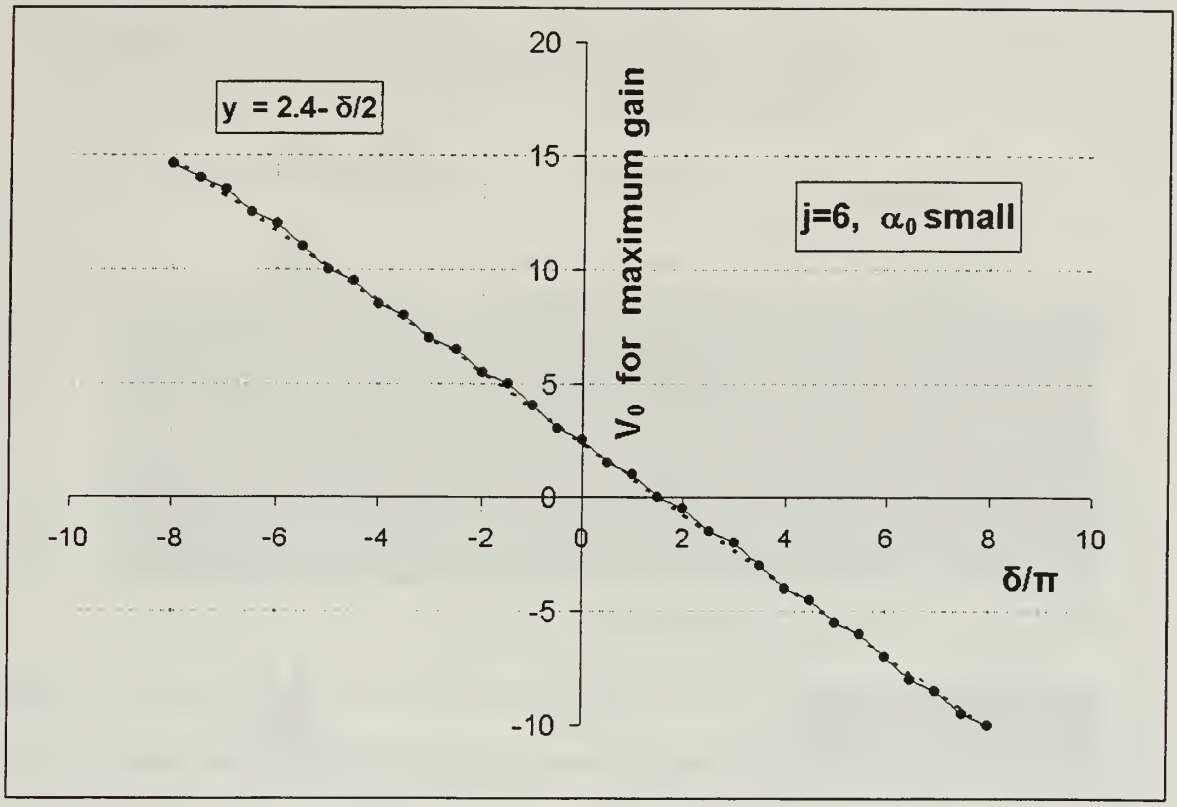

Figure 21. Position of Peak Gain versus taper.

B. MULTIMODE EVOLUTION OF SHORT PULSES

Multimode behavior is simulated by introducing a short parabolic electron pulse shape into the optical resonator and following the evolution of the optical pulse and optical mode as a function of the number of round trips n, through the resonator. Picosecond long electron pulses are often used in the FEL oscillator driven by an RF accelerator. At resonance, exactly one wavelength of light λ passes over an electron as the electron passes through one undulator wavelength λ_0. Over the whole undulator length, N

wavelengths of light pass over the slower electrons. We define the "slippage distance" as $N\lambda$ and is the distance that the electron pulse slips behind the faster optical pulse as they travel through the undulator. It is the characteristic length over which electrons and light can exchange information during the interaction in the undulator. When the electron pulse length is comparable to the slippage distance, then short pulse effects are important in the FEL interaction.

As short electron pulses enter the undulator, short optical pulses start from spontaneous emission and bounce between the resonator mirrors separated by a distance S, which is greater than the undulator length L. At $\tau=0$ the electron pulses from the RF accelerator enter the undulator, while the rebounding optical pulses arrive to overlap the electron in time intervals of $2S/c$, the round-trip bounce time of light in the resonator. We define "desynchronism" $d = -2\,\Delta S/(N\lambda)$ as the displacement between the electron and optical pulses at the beginning of the undulator ($\tau=0$) normalized to the slippage distance. In practice, d is adjusted by moving one of the resonator mirrors, thus altering the distance S.

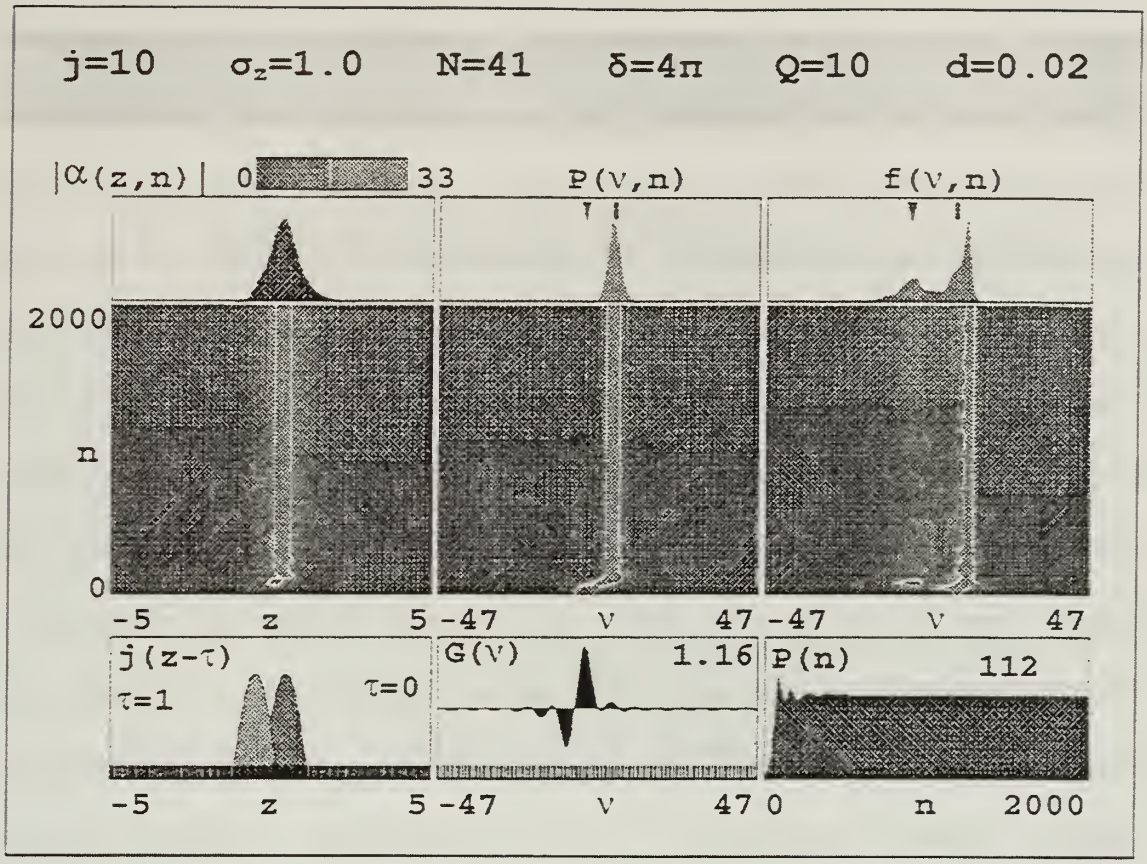

Figure 22. Short Pulse Evolution with δ=4π and d=0.02.

Figure 22 shows a sample simulation result after n=2000 passes with taper δ=4π. Several parameters are printed across the top; the peak current j, the resonator loss factor Q, the pulse width σ_z, also δ, and N. The upper graphs give the optical field shape $|\alpha(z,n)|$, the optical power spectrum P(ν,n), and the electron spectrum f(ν,n) at the final pass. The shading in the middle graphs show how these quantities have evolved with n. The scale ranges from 0 in black to the maximum value shown as gray. On the

bottom left, the longitudinal profile of the current density, or electron pulse $j(z-\tau)$ is shown for reference at dimensionless times $\tau=0$ (black) and $\tau=1$ (gray). The calculational window is 10 slippage distances long, and electron pulse slips behind one slippage distance in that window. The z parameter in this Figure is dimensionless $(z/N\lambda)$. The bottom center graph shows the weak-field gain spectrum for reference, and the right bottom graph shows the evolution of the total power $P(n)$. The power is the square of the dimensionless optical pulse amplitude α integrated over the pulse length. In this particular case, after going through some transients, the FEL reaches a steady state within approximately n=100 passes. Note the sudden shift of the optical power spectrum at $n \approx 100$; as n increases, the optical field strength grows and distorts the gain spectrum. As seen in Figures 16-19, the gain peaks at larger values of ν as the optical field α becomes large, causing the power spectrum to shift to larger values of ν.

Gain in weak fields is described by $G(\tau) = j\nu_0\tau^4 / 12$ so that there is no gain at the beginning of the interaction. This delay in gain is called "lethargy". At later times the electron pulse becomes bunched and the light pulse is

distorted because gain is preferentially deposited on the trailing edge of the pulse. The centroid of the light pulse travels slower than c. At exact synchronism (d=0) the electron and light pulses enter the undulator simultaneously. Surprisingly, the steady-state power of the FEL in this case is 0 because the light pulse drifts away from the electron pulse over many passes. Figure 23 shows the pulse evolution of such a case where the optical power evolves to zero after being started with an artificial pulse of light. Introducing a small value of desynchronism, we compensate for the slower speed of the light pulse and we find a better coupling of electron and optical pulses. Considerable power is achieved in the steady state, as shown in Figure 22.

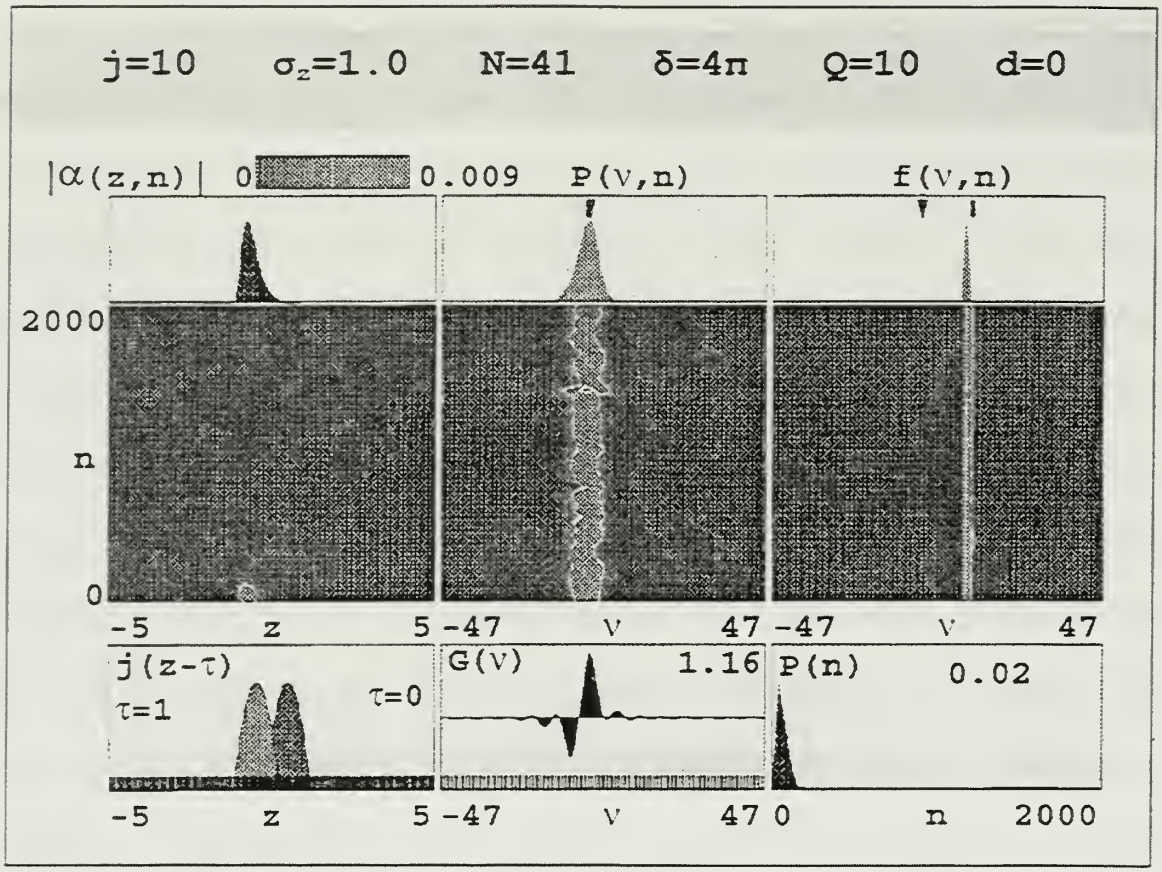

Figure 23. Short Pulse Evolution with δ=4π and d=0.

C. TRAPPED-PARTICLE INSTABILITY

In strong optical fields, electrons can become trapped in deep potential wells in phase space. The oscillation of the beam current that is trapped in these wells can drive the carrier wave unstable and cause sideband frequencies to grow from noise. As the FEL reaches high-power saturation, the height of the separatrix is large and many electrons are trapped in the closed orbits of phase space. Trapped

electrons execute synchrotron oscillation with the synchrotron or trapped-particle oscillation frequency $\nu_s \approx \left(|\alpha|^2 - \delta^2\right)^{\frac{1}{2}}$. Sidebands can appear around the fundamental at $\nu_0 \pm \nu_s$, and are shifted away from the fundamental wavelength by $\Delta\lambda / \lambda = \nu_s / 2\pi N$. The general features of trapped particle instability depend only on j and the loss factor Q. Increasing either j or Q can result in the trapped particle instability. The trapped particle instability usually occurs for small desynchronism, and has mixed effects in the FEL. Often, the experiment would like a high power laser that has a narrow spectrum and no sidebands. But the presence of sidebands means that high power has been obtained and the FEL is otherwise operating well. In fact, as more sidebands develop, even more power and higher efficiency are attained. Figure 24 presents the features of the trapped particle instability. The optical pulse (upper left) is short and partially modulated with sharp spikes. A small sideband is also evident at the optical power spectrum $P(\nu,n)$.

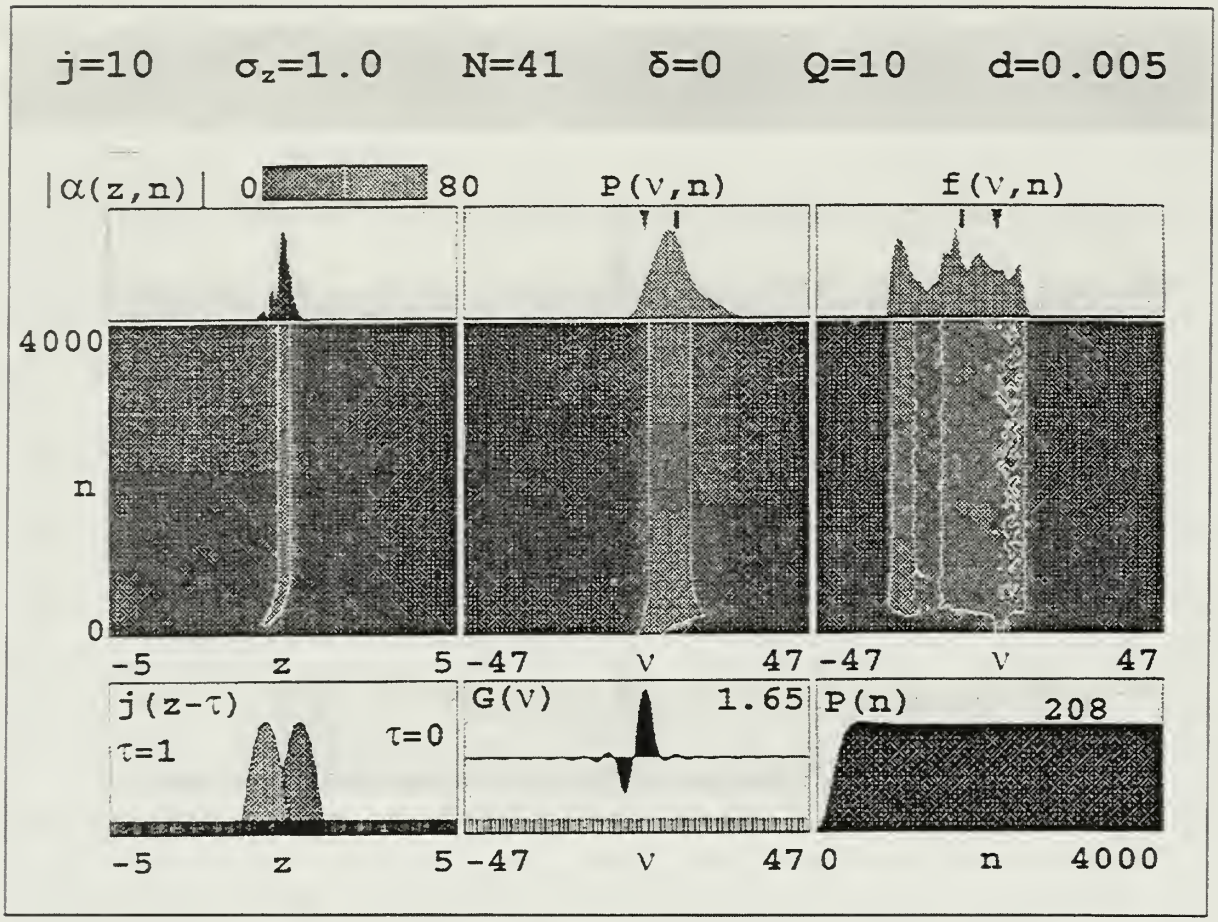

Figure 24. Trapped Particle Instability.

D. SIMULATIONS OF THE TJNAF FEL WITH A TAPERED UNDULATOR

Experiments using the TJNAF FEL have explored operation with both the tapered and inversely tapered undulators (Ref. 15 and 16). I present here the results of numerical simulations using the TJNAF experimental parameters. The TJNAF FEL has N=41 undulator periods of length λ_0 = 2.7 cm each. The undulator parameter is K= 0.98, the resonator loss factor is Q=10 (10% loss per pass), and the linear

taper rates are $\Delta K/K = 5\% (\delta = 4\pi)$, $7.5\% (\delta = 6\pi)$, and $10\% (\delta = 8\pi)$. Multimode simulations describe the evolution of short pulses in the far infrared, and show how positive tapering affects single pass gain, steady state power, and the electron energy spread as a function of desynchronism.

1. 34.5 MeV Electron Beam

In this case, the FEL was operated with short 0.5 ps electron pulses (length $l_e = 150\mu m$) of total energy E=34.5 MeV, with a 0.25% energy spread. The peak current was I=50 A, and the resulting optical wavelength is $\lambda = 6\mu m$. From these values, the dimensionless parameters where determined: j=10 (dimensionless current), and $\sigma_z = l_e / N\lambda = 1.0$ (electron pulse length). The goal was to determine the steady state power, the steady state gain in weak fields, as well as the electron energy spread as a function of both δ and d.

a) Steady State Power

Figure 25 summarizes the results of many simulations obtained using numerous values of desynchronism from d=0 to d=0.4, for taper rates δ= 0, ±4π, ±6π, and ±8π. The number of passes n in each simulation was sufficient for the optical power to evolve to steady state. The steady-state dimensionless power is plotted versus desynchronism, for different tapering rates δ, giving rise to the desynchronism curves.

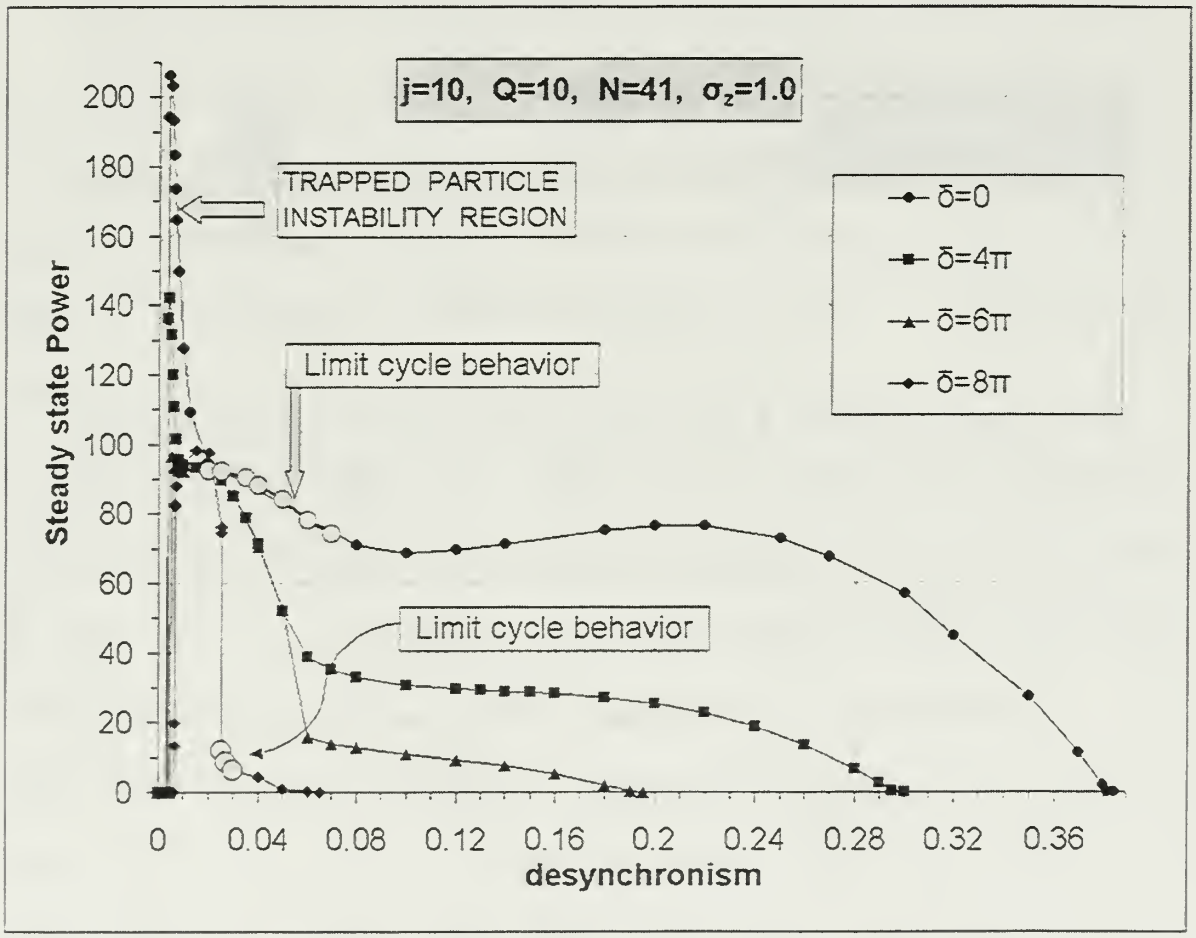

Figure 25. Desynchronism Curve for various tapering rates.

For values of d < 0.004, the laser does not operate. But at slightly large value of d, the power rises sharply. For small d, the gain is small so that a large number of passes n is required to achieve steady-state power. For $\delta=0$, the sharp peak in power at small desynchronism is accompanied by the trapped-particle instability. This effect is reduced as taper increases, since tapering tends to reduce the side bands. As the tapering rate is increased, the steady-state power decreases and the peak power of each curve moves slightly to larger values of desynchronism. The conventional undulator is more efficient than the tapered undulators. Furthermore, higher tapering rates reduce the range of desynchronism values where the laser works. For no tapering, the FEL works for values of desynchronism as big as d=0.38. However, a tapering rate of $\delta=8\pi$ reduces the range to only $\Delta d=0.19$. For $\delta=0$, the power peaks at d=0.004 with the trapped-particle instability. This is expected since the sidebands contribute significantly to the final power. For $\delta=8\pi$, the steady-state power is 50% smaller and peaks at d=0.015. For larger d, the power diminishes significantly as the taper increases. The flat sections of the desynchronism curves

are desirable regions to operate the FEL, since they are predictable and stable. Limit-cycle behavior is observable for $\delta=0$ between $d=0.02$ and $d=0.07$, and for $\delta=8\pi$ between $d=0.025$ and $d=0.03$. For these regions, shown on the graph as large circles, only the peak power of the steady state power is shown. Limit-cycle behavior causes oscillations of the power $P(n)$, the power spectrum $P(\nu,n)$, and the electron spectrum $f(\nu,n)$. The steady-state power oscillates periodically by as high as 50%, between the peak and the low values. Limit-cycle behavior occurs when trapped particles in strong fields combine with short optical pulses. The modulation caused by the oscillation of the trapped current continually modifies the shape of the short optical pulse. The different pulse shapes have different powers P and spectra $P(\nu)$, causing oscillations as subpulse structures march through the optical pulse envelope. Figure 26 shows an example of limit cycle behavior for $\delta=8\pi$ and $d=0.026$.

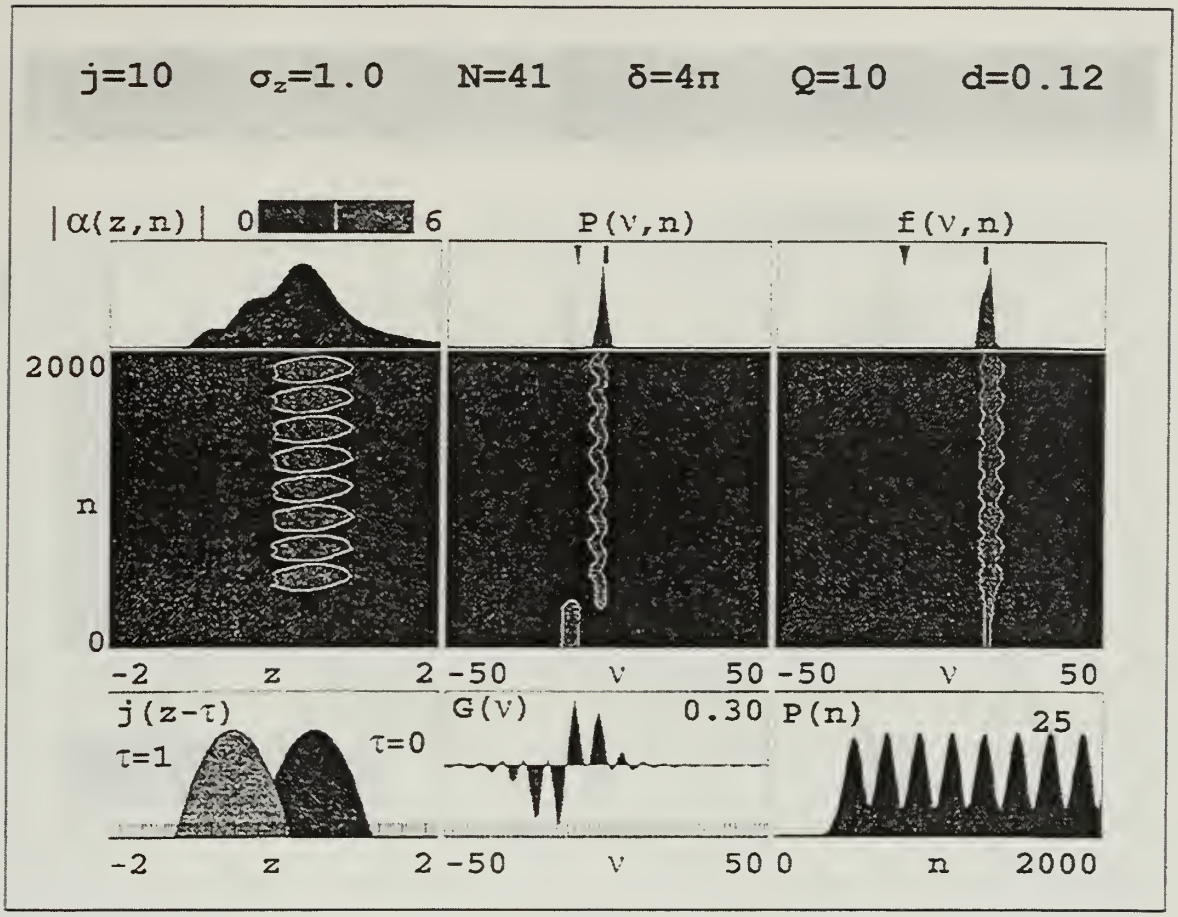

Figure 26. Limit-cycle behavior.

b) Steady State Gain

In order to determine the steady-state, weak field gain as a function of desynchronism, the same simulations were used. Instead of plotting power as a function of n in the lower right graph of each simulation output, P(n) is replaced by gain G(n), as shown in Figure 27. The simulation was run only long enough for gain to reach a steady-state value.

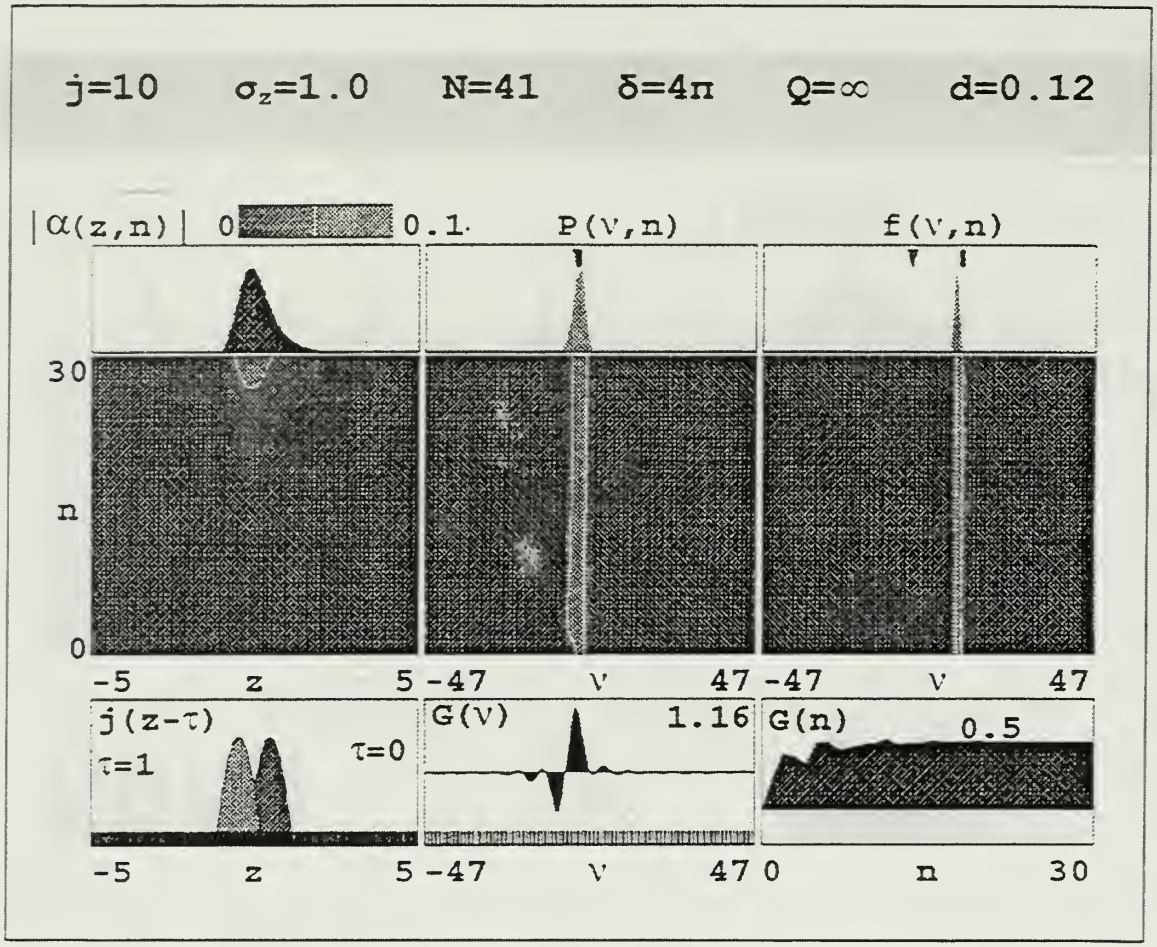

Figure 27. FEL Short Pulse and Gain Evolution.

Since we are interested in the weak field gain, the optical field α must be kept less than unity by starting with an initial optical field $\alpha_0 \approx 10^{-5}$. The loss factor is $Q = 10^{10} \approx \infty$, so that the mirror losses (1/Q) would be negligible. The power and electron spectra are narrow, since the optical field is small.

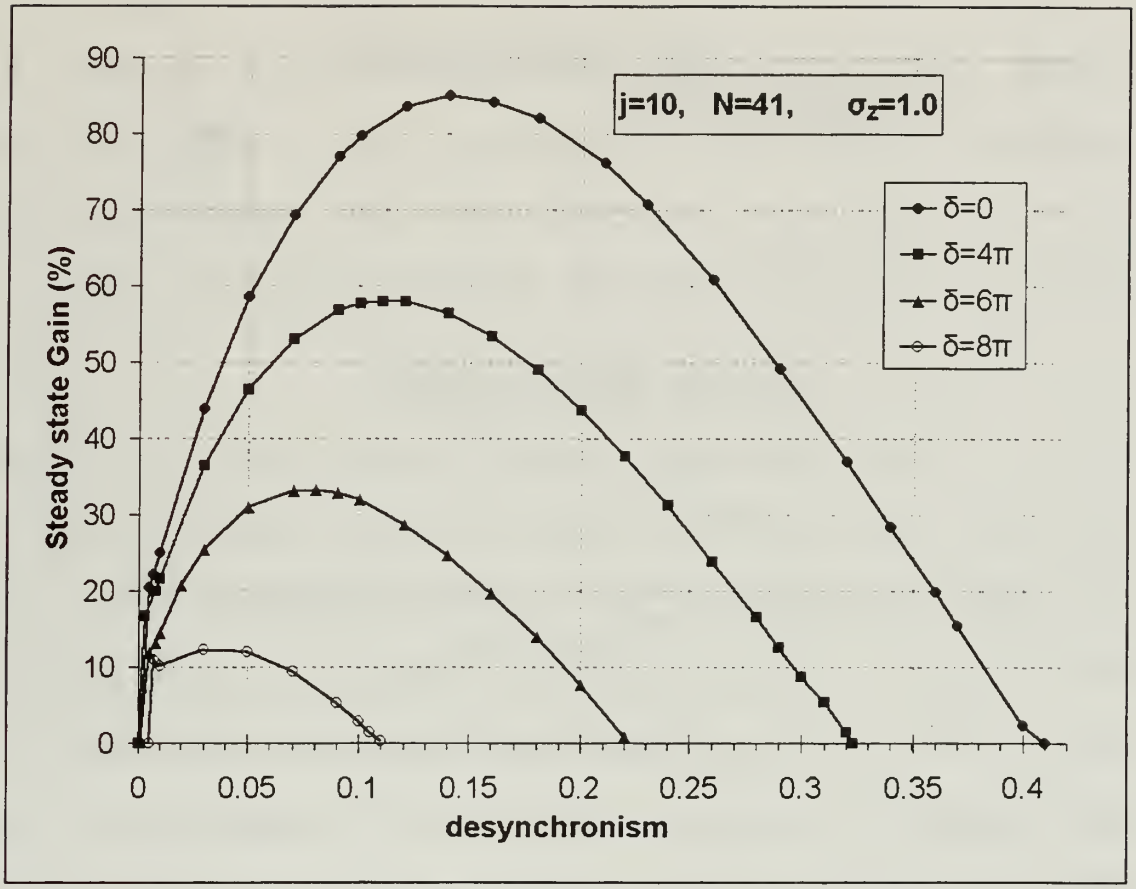

Figure 28. Steady State Gain versus desynchronism

In Figure 28, the weak-field, steady-state gain is plotted as a function of desynchronism d, for the given tapering rates δ. Clearly the gain curves are much different from the desynchronism curves and peak for moderate values of d. When tapering increases, the peak gain of each curve shifts to smaller values of d. For no tapering (δ=0), the peak gain is 85%, at d=0.14. When δ=8π, the peak gain drops to only 12%, at d=0.03. The most

common feature of the desynchronism curve is that the operating range, (Δd), decreases as δ increases. Note that when the gain drops to Q=10%, the final power drops to 0 because the FEL loss per pass exceeds the gain per pass.

c) Electron Energy Spread

When the power reaches steady state, we measure the full width $\Delta\nu$ of the final electron spectrum, which is the upper right graph of the computer simulation output (see Figure 24). From $\Delta\nu$ we can determine the fractional electron energy spread using $\Delta\gamma/\gamma = \Delta\nu / 4\pi N$ where N=41. In the TJNAF EEL design, the electron beam exiting the undulator is redirected by bending magnets and fed back into the accelerator. This recirculation allows energy recovery from the electron beam, and significantly increases the FEL efficiency. The induced electron energy spread is crucial to this process, because beam recirculation is feasible only if the full electron energy spread is less than 6%. In Figure 29, the fractional electron spread induced by the FEL interaction is plotted as a function of d and δ. The curves appear much like the power curves in Figure 25 with initial sharp peaks of 7%-8% near d=0.01. However for d >0.025, all the energy spreads are less than 6%.

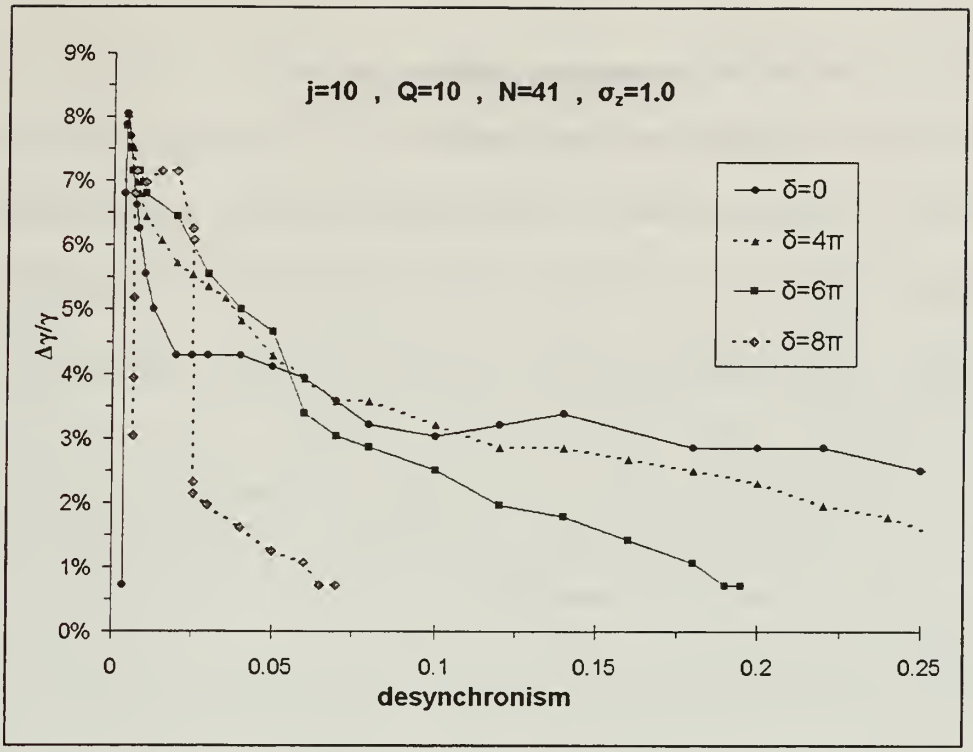

Figure 29. Electron Energy Spread.

Between d=0 and d=0.05, where we have the maximum output power, the induced energy spread is significantly smaller for the conventional undulator than the tapered one. For d=0.025, the energy spread was 4.5% for the untapered undulator and around 6% for all the other tapers. The tapered undulator does not appear to be desirable for recirculating the electron beam. After d=0.05, the energy spread drops to less than 4% for all the tapering rates. With short optical pulse, the head and tail of the pulse have weak optical fields, so that tapering is not optimum along the pulse. This is the reason the energy spread is greater in the tapered undulators.

2. 47.5 MeV Electron Beam

a) Steady-State Power

In this case, the dimensionless parameters are defined: j=7 and $\sigma_z = 1.8$. The optical wavelength was $\lambda = 3\mu m$. The desynchronism curves were again determined as shown in Figure 30. The curves are very similar with those using the 32.5 MeV (Fig. 25). However, the operating ranges and the final power are smaller because of the smaller value of j. For taper $\delta=8\pi$, the laser barely works.

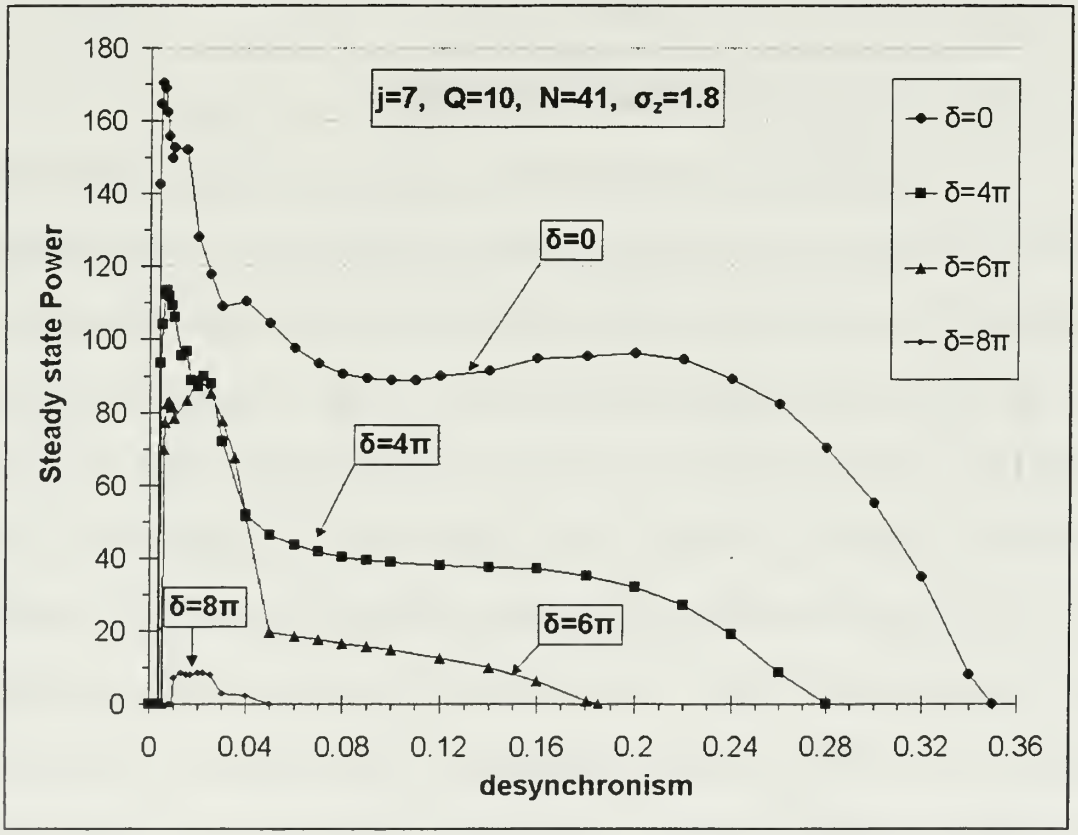

Figure 30. Desynchronism Curve for 47.5 Mev electron beam and various tapering rates.

The operating width of the desynchronism curves, Δd, as a function of taper has been measured in experiments conducted with the IR Demo FEL at Jefferson Lab [Ref 16]. The FEL parameters used in the simulations were the same as those of the experiments (λ = 3μm, N=41, Q=10, j=7 and σ_z = 1.8). In Figure 31, the relative width of the desynchronism curve is plotted as a function of taper, using both experimental and computer simulation data. The relative width is the maximum value of desynchronism where the FEL operates for each taper, divided by the width of the desynchronism curve of the untapered undulator (δ=0). Both simulations and experiments show that the operating range decreases as the taper increases. There is good agreement between theory and experiment.

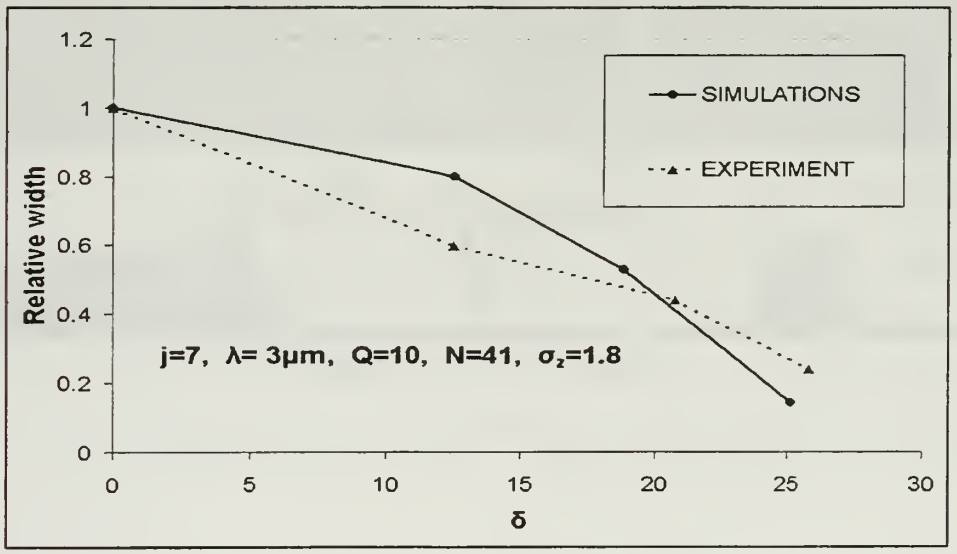

Figure 31. Relative width of desyncronism curve versus taper δ.

The trapped-particle instability and limit-cycle behavior were again characteristic features of the simulation results. Figure 32 presents the simulation output with j=7 and σ_z = 1.8 (47.5 MeV Energy), δ=0, and d=0.025. The simulation was run only for n=300 passes in order to better present the details. The oscillation of the total power, the optical pulse distortion and the sideband in the optical power spectrum are clearly shown.

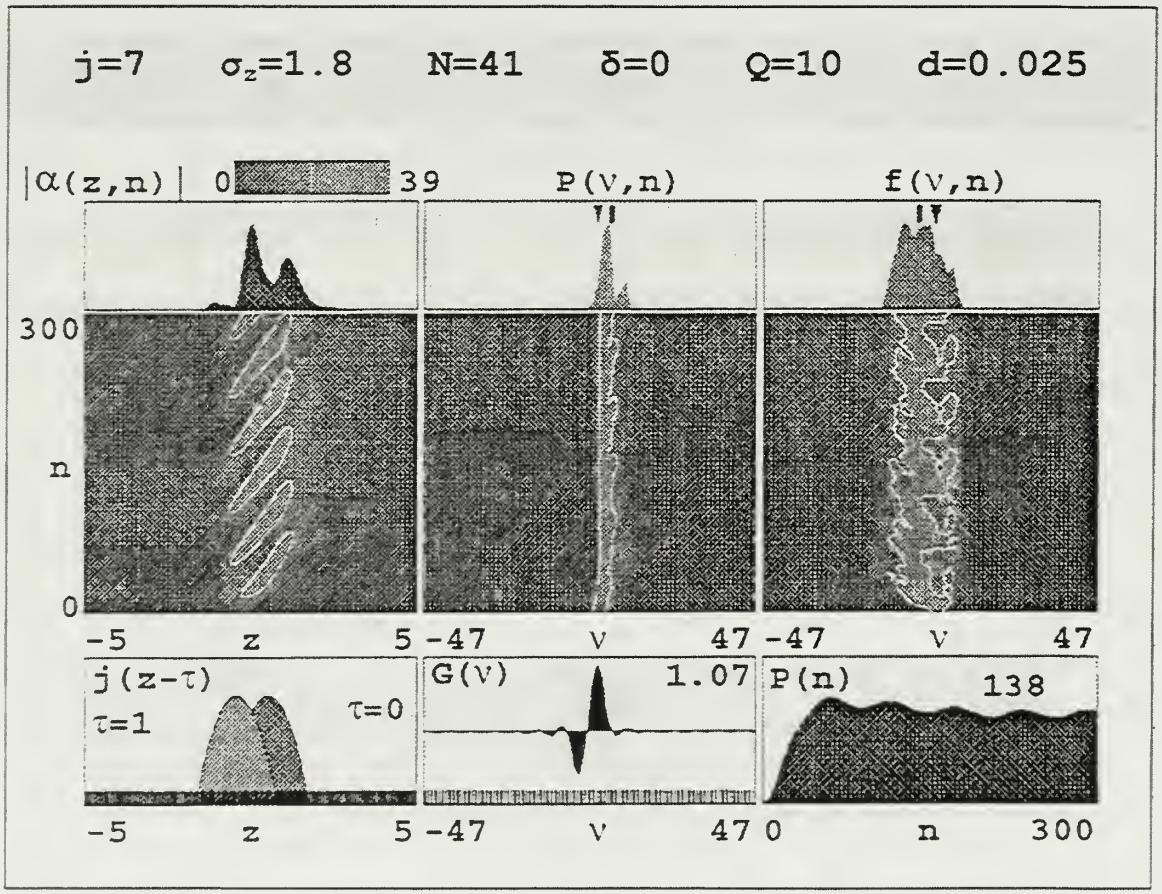

Figure 32. Simulation Output for d=0.025 and δ=0.

Limit-cycle behavior in the final power was observed for $\delta = 0, 4\pi, 8\pi$ and not for $\delta = 6\pi$. Figures 33-35 show the desyncronism curves of Figure 30 in order to more clearly presentthe details of limit-cycle behavior.

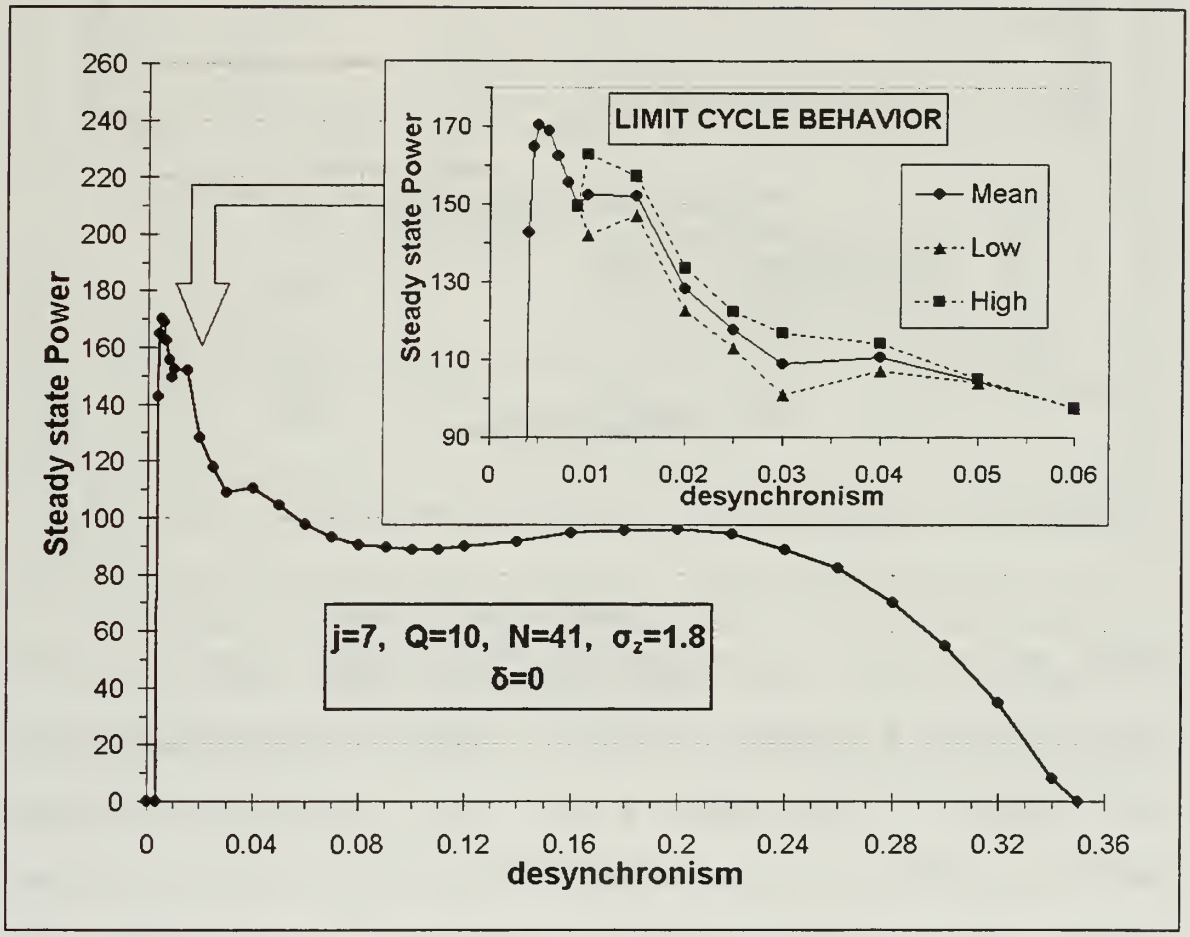

Figure 33. Desynchronism Curve for $\delta=0$.

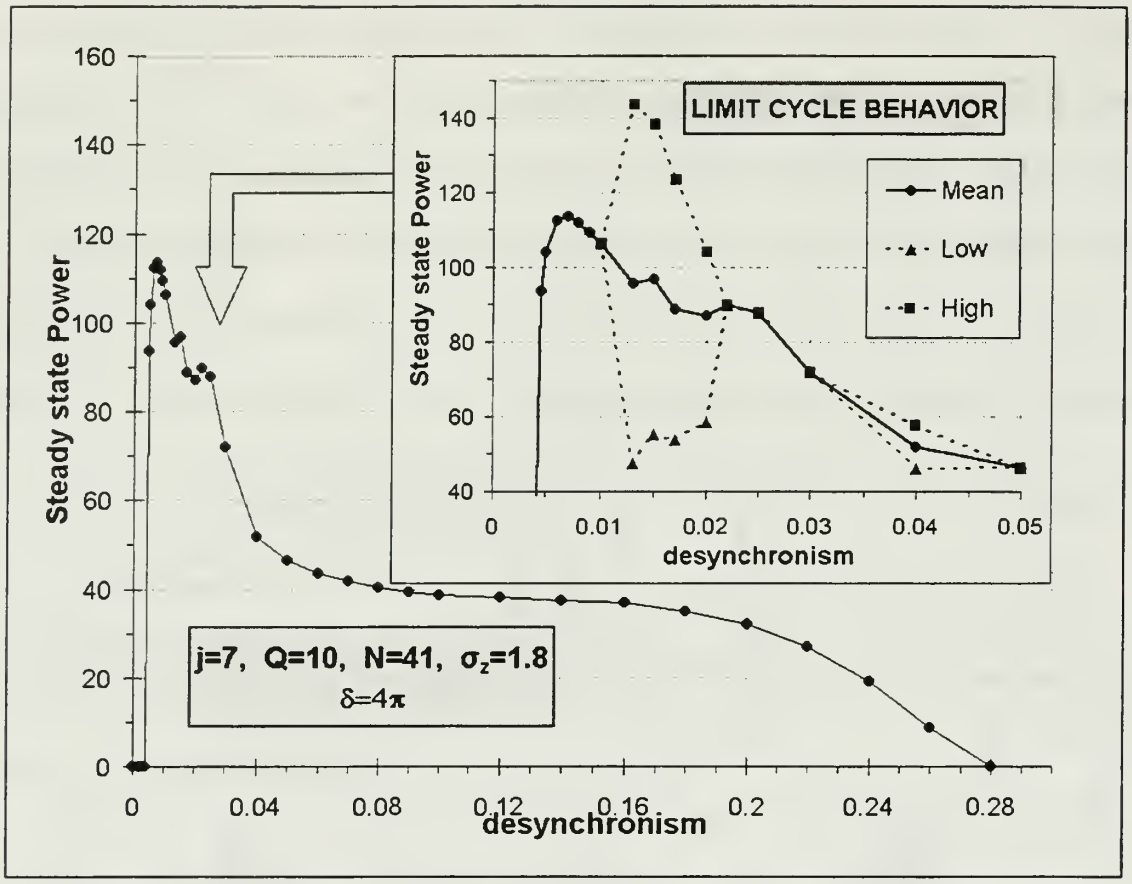

Figure 34. Desynchronism Curve for δ=4π.

The upper right graphs of Figures 33 and 34 show blown up section of the desynchronism curve section where the limit-cycle behavior occurs. Since there are periodic oscillations of the total power, the maximum and minimum power is indicated in the graph. The mean power is the average of the maximum and the minimum. The desynchronism curves in Figure 30 plotted the mean power. Figure 35 shows the desynchronism curve for δ=8π, emphasizing the limit-cycle behavior.

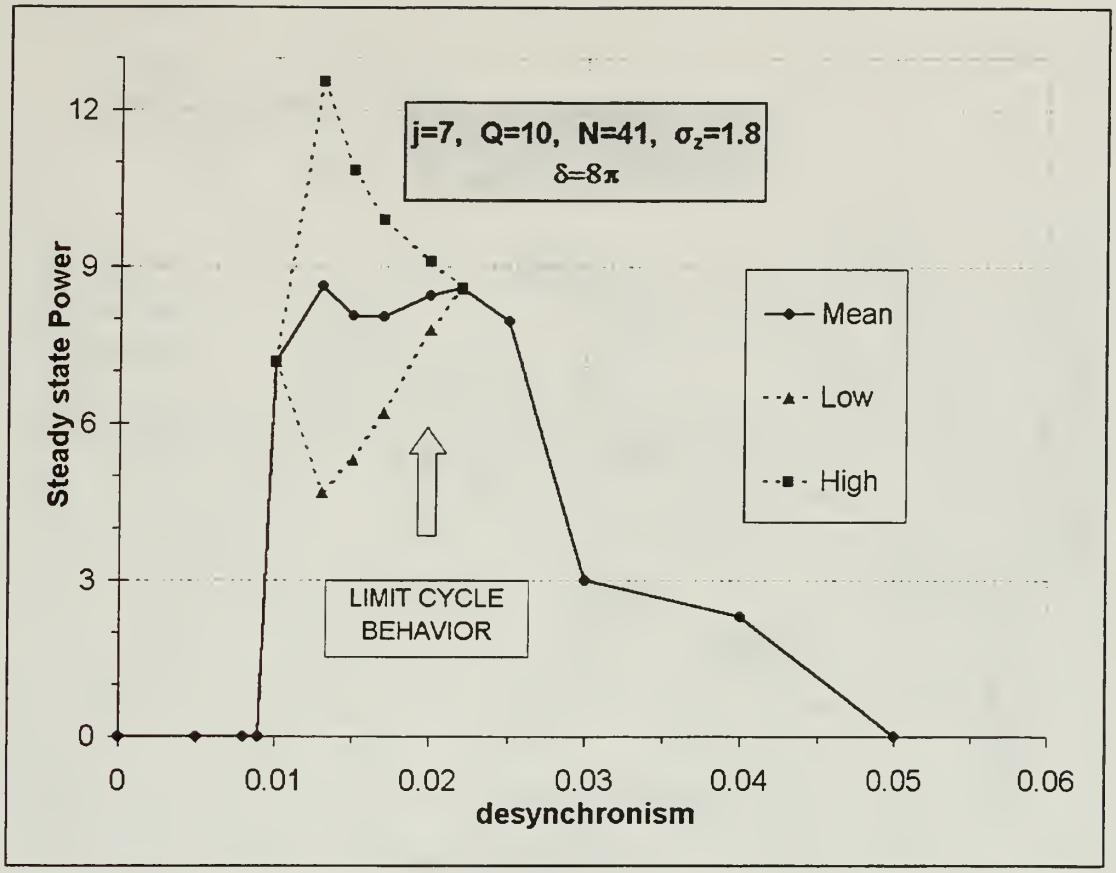

Figure 35. Desynchronism Curve for δ=8π.

b) Steady-State Gain

The same procedure as the one followed in paragraph 1b was followed in order to determine the steady-state, weak-field gain as a function of taper and desynchronism. The results are presented in Figure 36 and are similar to those with the 32.5 Mev beam energy (Figure 29). Still the operating ranges, as well as the gains, are smaller.

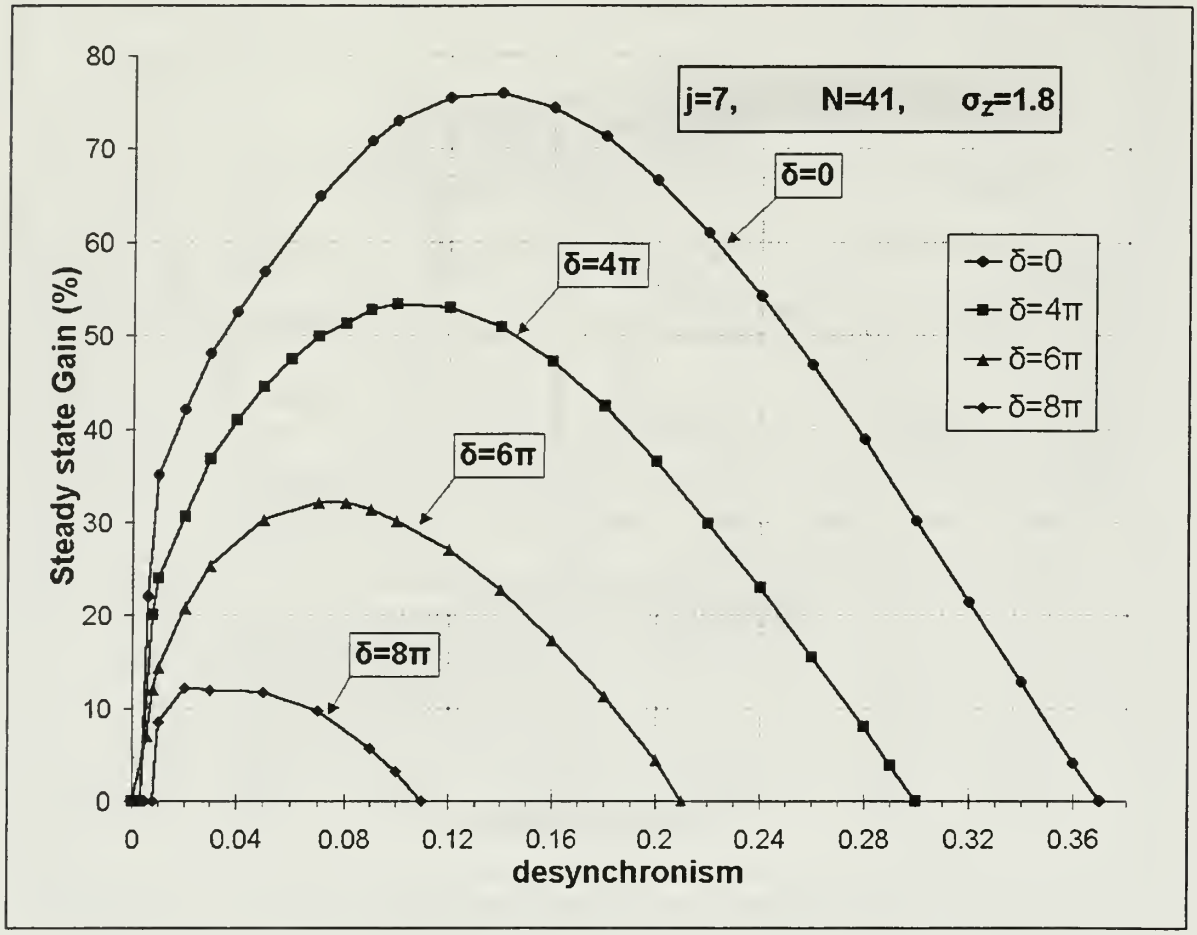

Figure 36. Steady State Gain versus desynchronism for 47.5 Mev electron beam.

c) Electron Energy Spread

Figure 37 shows the fractional electron spread as a function of d and δ. The results are again similar to those with 32.5 MeV electron beam energy. The curves have the same trend as the power curves (Fig. 30) with a peak near d=0.01. The peak fractional energy spread is approximately 1% smaller than for the 34.5 MeV beam because of the smaller value of j.

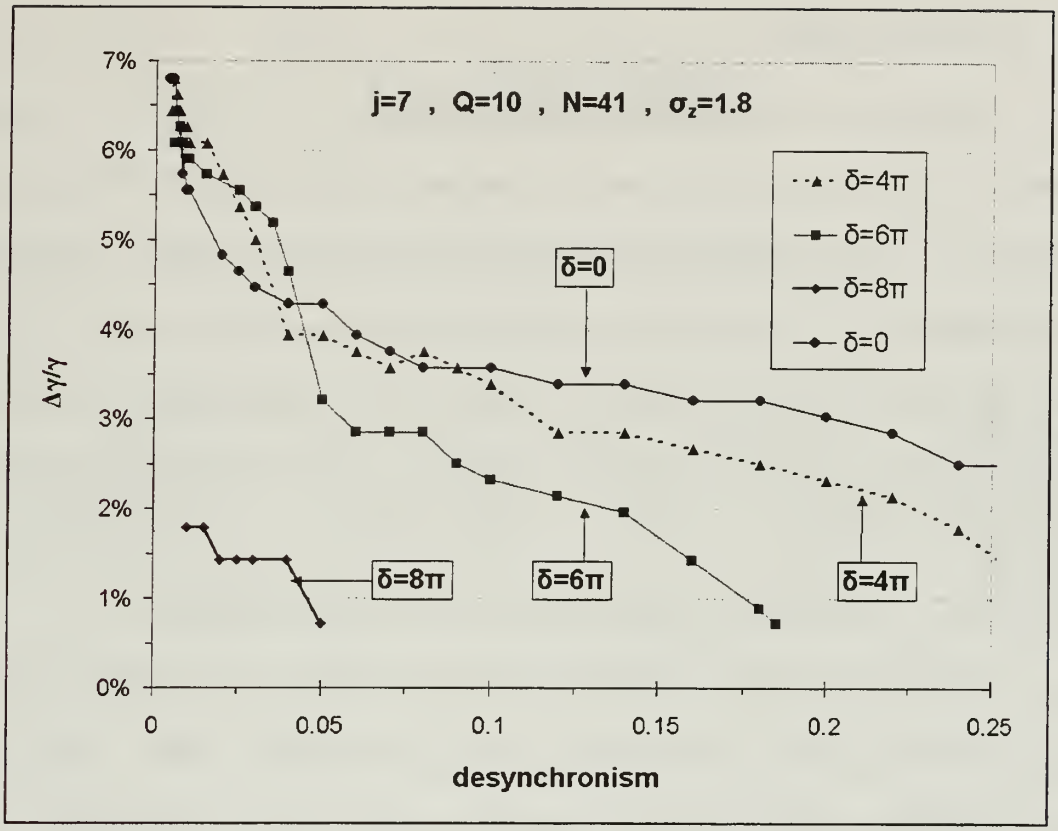

Figure 37. Electron Energy Spread for 42.5 MeV Electron Beam.

Initial peaks of 7% induced energy spread are evident at the start up region (d=0.007). For d > 0.015, the energy spread drops to less than 6%, implying the possibility of beam recirculation. In the region of high steady-state power(0.01< d <0.04) the conventional undulator (δ=0) has almost 1% less energy spread than the tapered (δ=4π,6π). Thus, the untapered undulator is a better candidate for beam recirculation. The short optical pulses, with weak fields at the head and tail, cannot be easily designed to reduce energy spread.

E. CONCLUSIONS

Experiments were conducted with the TJNAF IR demo FEL (Ref. 16) in order to test its operation with various taper rates δ, and desynchronism values using the following parameters:

Undulator Periods	N	41	41
Wavelength	λ	3μm	6 μm
Electron Beam Energy	E	47.5 MeV	34.5 MeV

Table 3. Parameters used in the FEL experiments.

In this thesis, computer simulations were used in order to explore the operation of the TJNAF FEL with the conventional and several tapered undulators using the same parameters as in experiments. The corresponding dimensionless parameters used in the simulations are listed in Table 4.

Electron Beam Energy	E	47.5 MeV	34.5 MeV
Dimensionless Current	j	7	10
Resonator loss factor	Q	10	10
Pulse length	σ_z	1.8	1.0

Table 4. Parameters used in the simulations.

The desynchronism curves were determined at each electron beam energy, and present a sharp peak at small values of desynchronism accompanied by the trapped-particle

instability. Trapped-particle instability was reduced for larger values of taper, since tapering suppresses the sidebands. Limit cycle behavior was also observed for most tapering rates. Although the general shape of the curves is very similar for each beam energy, the final power and gain were significantly smaller for the 47.5 MeV electron beam than for the 34.5 MeV electron beam, because of the lower value of j.

The tapered undulator turned out to be less efficient than the conventional undulator, demonstrating reduced gain and power, and increased energy spread to the electron beam.

The width of the desynchronism curve decreased as the tapering rate is increased, in agreement with the experiments. A publication is being prepared comparing the experimental (Ref. 16), and simulation results.

THIS PAGE INTENTIONALLY LEFT BLANK

V. EXPERIMENTAL RESULTS OF DAMAGE INDUCED TO MATERIALS BY THE TJNAF FEL

A. LASER MATTER INTERACTION

The interaction between lasers and matter is a complicated issue generally described by non-linear and unpredictable effects. The laser beam has the unique ability to deliver very high power per unit area. When high power laser radiation falls on a target, the part of the beam that is absorbed begins to heat the target surface very rapidly to its melting temperature. This melting process then penetrates progressively into the material. Many physical processes govern the damage caused to the material by the laser power including power absorption, power reflection, heat conduction, and heat diffusion. Furthermore, a large number of parameters play a major role in these processes such as material density and heat capacity, as well as the irradiation wavelength, power density, peak power, and possibly pulse characteristics.

A good knowledge of these mechanisms helps one understand the capabilities and limitations of the directed energy, and allows better control of the damage caused by the laser. Controlled damage has many industrial

applications such as the creation of thin coatings, electronic component fabrication, precise drilling, cutting, etc. However, when using the high-power laser as a weapon to shoot down missiles, precision and symmetry of the damaged area are not the issue. Our goal is to cause the maximum possible damage on a rapidly moving missile; this requires precise tracking of the laser beam through a turbulent atmosphere

B. SCALING

As stated in chapter III, an intensity of 10 kW/cm^2 over a 6 cm radius spot for a few seconds dwell time is needed to burn an adequate hole in a missile. In these damage experiments, the TJNAF FEL used only several hundred watts. In order to achieve the desired intensity of 10 kW/cm^2, the laser beam has to be focused with a lens to a much smaller spot size. For average power P and spot area A, the resultant intensity is $I = P/A$. Given a specific power, we can adjust the spot size to achieve the desired intensity. Studying a spot radius on the order of 0.1 cm and using 500 W power, we can achieve 10 kW/cm^2 intensity. The goal of this scaling is to develop guidelines that will

reliably predict the damage caused by a high power laser over a large area.

Nevertheless, the spot size cannot be arbitrarily small, or the scaling will not work. Each material is characterized by a parameter called the thermal diffusion length D, which represents the distance required for the temperature to drop by a factor of 1/e, and determines the ability of the material to absorb and transport heat. If D is greater than the laser beam spot size diameter, the heat deposited by the laser beam will diffuse away in less time than it takes the material to melt. In order to obtain effective heating, and cause melting of the material irradiated, the thermal diffusion length should be smaller than the beam diameter. Also, the damage hole cannot be much greater than the laser beam radius. Material cannot easily escape a deeply damaged hole, and the damage mechanism may be complicated by the material ejecting the hole and flowing through the beam.

C. EXPERIMENTAL PROCEDURE

The sample materials used in the experiments were Polyimide Fiberglass and F2 Epoxy. The samples provided by the Naval Research Laboratory are the same as those used in

similar experiments conducted in March 1999. The results of the March 1999 irradiations, which involved three holes in each sample labeled 1,2, and 3, were presented in Reference [14], and some of them will be mentioned in this thesis. The results presented by this thesis were obtained by two different experiments conducted in August 1999 and March 2000. The results from both experiments will be presented together in order to make the analysis more comprehensive.

1. August 1999 Experiment

Each sample was irradiated 12 times (4 sets of 3 irradiations with the same parameters) with a FEL beam of wavelength λ=3.1 μm, pulse repetition frequency 18.7 MHz and average power P=100W±5W. The Polyimide Fiberglass was irradiated first, followed by the F2-Epoxy. Measurements were made with samples placed downstream of a calcium fluoride lens with a measured back focal length of 137.6 mm for 3 μm wavelength. A camera was set up to observe the front and back surface of the samples. Two sets of three irradiations were first made. The average intensity was 500 W/cm^2, which was achieved by focusing the beam to a spot of 0.25 cm radius. Three identical irradiations were made initially with no airflow. Then three more irradiations were

made with a wind speed of 60 mph across the front face of the samples. Then, adjusting the beam radius to 0.087 cm, the intensity was set to I=10 kW/cm^2 and the same set of measurements were repeated.

2. March 2000 Experiment

The goal of these measurements was to maintain the average intensity of 10 kW/cm^2, but using higher laser power with a larger spot size. Each sample was again irradiated 6 times (2 sets of 3 irradiations) with a FEL beam of wavelength λ=3.1 μm, pulse repetition frequency 37.425 MHz and average power P=500W±10W. The Polyimide Fiberglass was irradiated first, followed by the F2-Epoxy. Measurements were made with samples placed downstream of a calcium fluoride lens with a measured focal length of 235.7 mm for 3 μm wavelength. A camera was again set up to observe the front and back surface of the samples. Irradiations were made with I=10 kW/cm^2 average intensity, which was achieved by focusing the beam to a spot of 0.13 cm radius. Three identical irradiations were made with no airflow, and then three more irradiations with a wind speed of 85 mph across the front face of the samples.

D. RESULTS

1. Sample #1 - Polyimide Fiberglass

The sample had dimensions 11.4 cm by 10.1 cm with 2 mm thickness. In Figure 38, we see a photo of the front side of the Polyimide Fiberglass sample after all sets of irradiations. Irradiations labeled by numbers 1,2 and 3 were conducted in March 1999. Irradiations labeled 4 to 15 were conducted in August 1999, and 16 to 21 were conducted in March 2000. All irradiations were done three times with the same parameters in order to get more accurate measurements. The actual results came from the mean value of the three measurements. Irradiations 7,8,9,10,11,12,16 17 and 18 were done with no airflow, while in 4,5,6,13,14,15,19,20, and 21 there was wind present. In Figure 39, we see a photo of the backside of the Polyimide Fiberglass sample showing that all of the irradiations with intensity of 10 kW/cm^2 completely penetrated the sample. On the other hand, the irradiations with an intensity of 500 W/cm^2 (irradiations 10 to 15 of Figure 38) did not penetrate the sample. Irradiation results are summarized in Table 5. Each row represents a set of three irradiations.

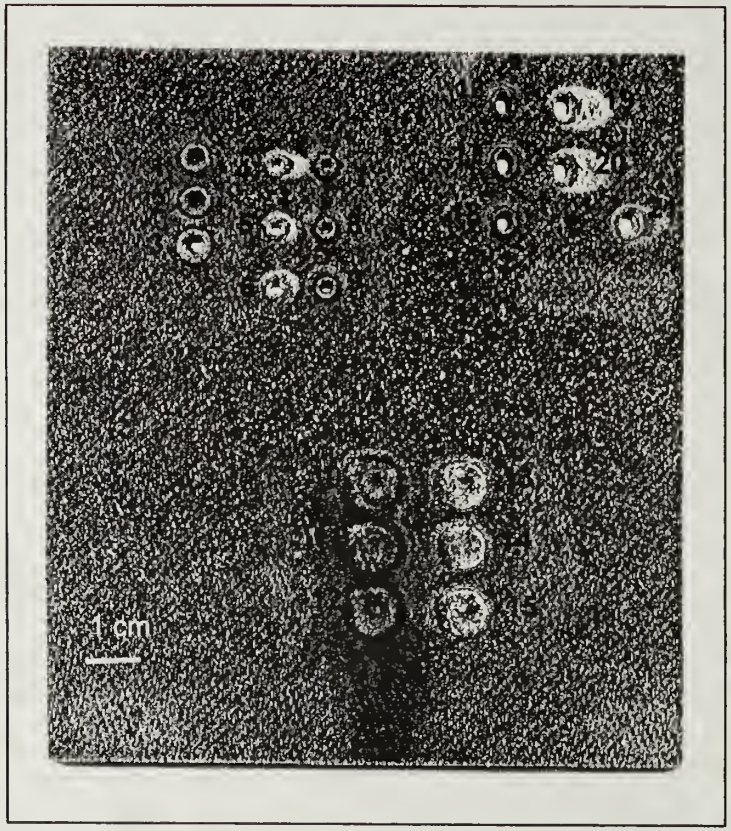

Figure 38. Polyimide Fiberglass (front view).

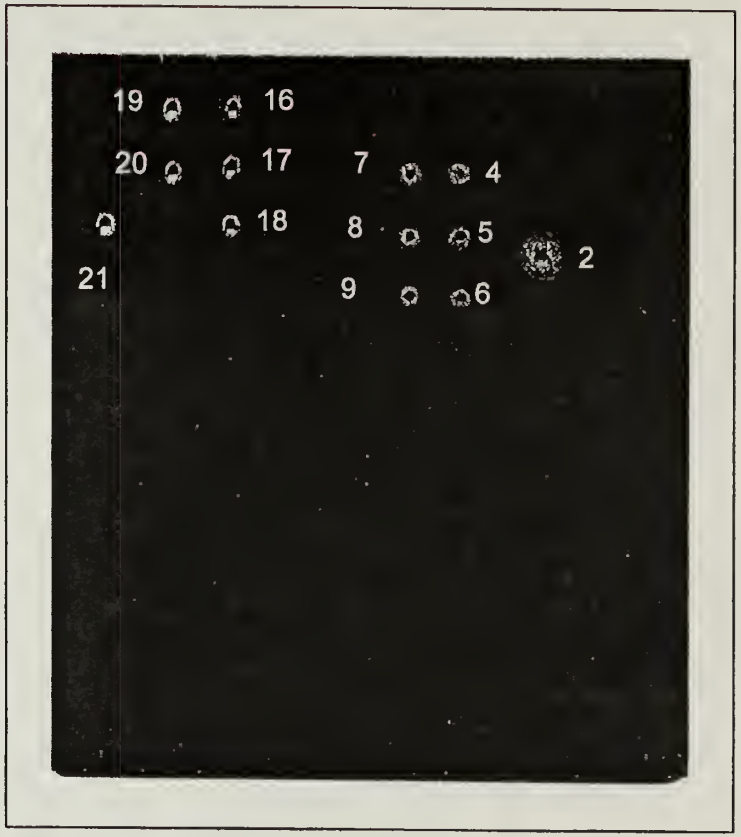

Figure 39. Polyimide Fiberglass (back view).

Hole Number	Average Power (W)	Average Intensity (kW/cm^2)	PRF (MHz)	λ (μm)	Spot radius (mm)	Wind (mph)	Burn through time (sec)	Penetration Depth Rate (mm/sec)	Front Damage Pattern	Entry Hole Diameter (mm)	Rear Damage Pattern	Exit Hole Diameter (mm)
10,11,12	100	0.5	18.7	3.1	2.5	NO	4.5 *	0.3	Circular	4.4	---	---
13,14,15	100	0.5	18.7	3.1	2.5	60	4.5 *	0.3	Circular	6.6	---	---
7,8,9	100	10	18.7	3.1	0.87	NO	1.4	1.4	Circular	1.7	Circular	1.3
4,5,6	100	10	18.7	3.1	0.87	60	1.2	1.6	Circular	1.9	Circular	1.4
16,17,18	500	10	37.4	3.1	1.25	NO	0.40	5.0	Elliptical	3.5 x 2.5	Elliptical	2.5 x 1.5
19,20,21	500	10	37.4	3.1	1.25	85	0.35	5.7	Elliptical	3.7 x 2.9	Elliptical	2.6 x 1.7

Table 5. Polyimide Fiberglass irradiations results.

* There was no burn through. The time indicated is the exposure time.

The hole diameters have variation of 15% in each set of three holes. This is due to the slight variation of the exposure time, which is on the order of 1-2 seconds.

The presence of airflow resulted in ≈15% bigger hole diameter and penetration depth rate, than those attained without airflow. The irradiations conducted with 500 W average power (runs 16 to 21), caused 3.5 times higher penetration depth rate than the ones conducted with 100 W, and the same intensity (kW / cm^2). This is probably because the higher power allowed larger spot, so that damaged material could more easily escape the larger damage hole.

The damage pattern of runs 16 to 21 is not circular as expected but somewhat elliptical, which is very clear in Figures 44, 45,46 and 47. The following figures present a closer caption of the damage caused by the irradiations.

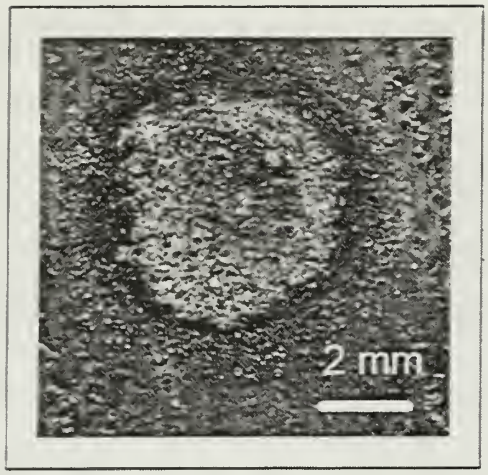

Figure 40. Polyimide hole 12.
Intensity 500 W / cm^2, no air.
Average Power 100 W.
Spot Radius 2.5 mm.

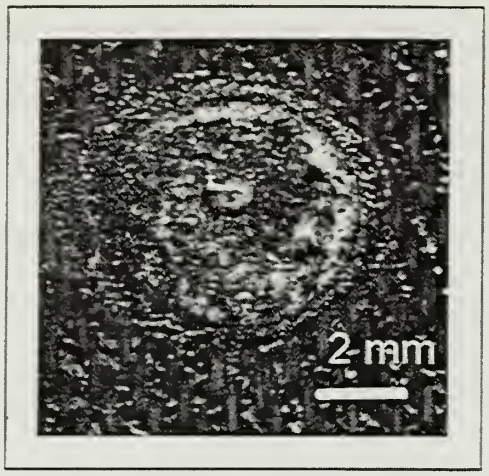

Figure 41. Polyimide hole 15.
Intensity 500 W / cm^2 with air.
Average Power 100 W.
Spot Radius 2.5 mm.

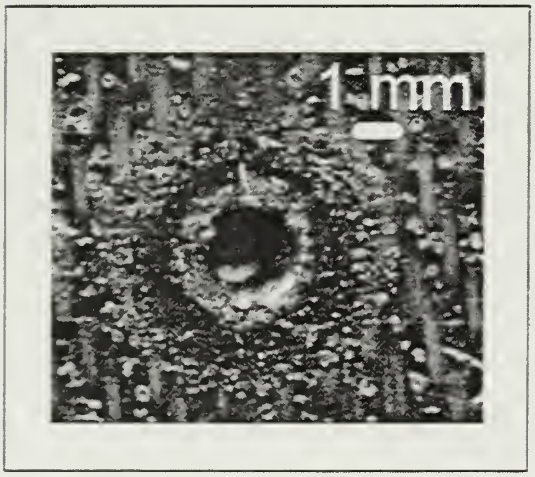

Figure 42. Polyimide hole 8.
Intensity 10 kW / cm^2, no air.
Average Power 100 W.
Spot Radius 0.87 mm.

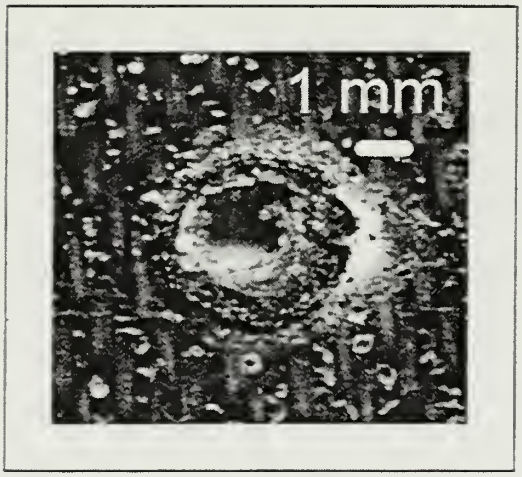

Figure 43. Polyimide hole 5.
Intensity 10 kW / cm^2, with air.
Average Power 100 W.
Spot Radius 0.87 mm.

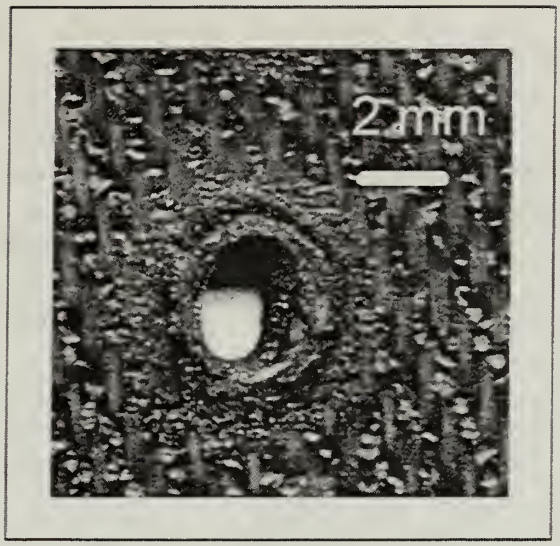

Figure 44. Polyimide hole 18.
Intensity 10 kW / cm^2, no air.
Average Power 500 W.
Spot Radius 1.25 mm.

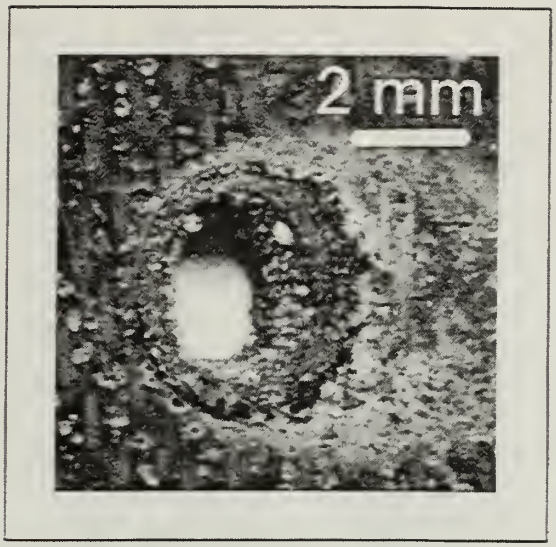

Figure 45. Polyimide hole 20.
Intensity 10 kW / cm^2, with air.
Average Power 500 W.
Spot Radius 1.25 mm.

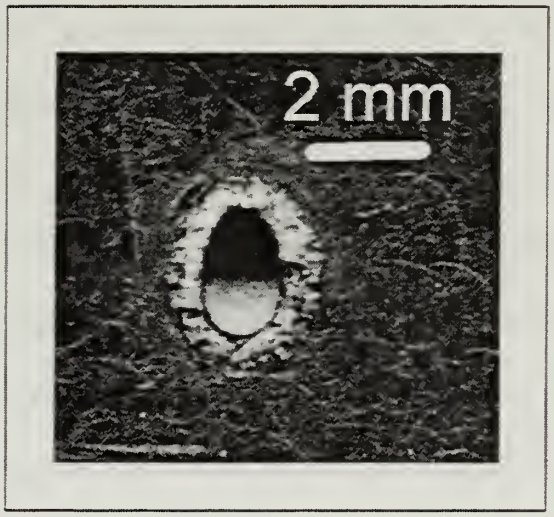

Figure 46. Polyimide exit hole 18.
Intensity 10 kW / cm^2, no air.
Average Power 500 W.
Spot Radius 1.25 mm.

Figure 47. Polyimide exit hole 20.
Intensity 10 kW / cm^2, with air.
Average Power 500 W.
Spot Radius 1.25 mm.

In all cases a raised lip of melted material is observed around the face of the entrance hole. The dimensions of the lip are approximately 0.2 mm height and 1 mm width. However, when airflow is present the lip tends to be smaller, possibly because the airflow removes the debris, and the evaporated material that actually contributes to the formation of the lip. That would explain the bigger diameter of the holes made in the presence of wind, since the diameter is measured from the inside part of the lip.

The charred region extends approximately 2 mm around the lip when there is no wind. With wind this area is much smaller. The charred region around the exit hole extends to 1 to 1.5 mm in all cases, as the backside of the sample was not exposed to the airflow. As exposure time increased the radial extent of the damaged area increased and more melted material was deposited around the hole. After the irradiation stopped, there was a period of almost 3 sec that the material is still hot and melting. The wind tends to cool down the material, decreasing this time almost in half and resulting in less melted material.

Investigation with a microscope reveals that there is no evidence of melted or rehardened material inside the

holes. It is also evident that the damage is most significant in the center of the hole, diminishing radially outward, which supports expectation of a Gaussian shape of the laser beam intensity.

The following table presents the results of the experiment conducted in March 1999 (Holes 1,2,3).

Average Power (W)	Average Intensity (kW/cm^2)	PRF (MHz)	λ (μm)	Spot radius (mm)	Wind (mph)	Penetration Depth Rate (mm/sec)
100	10	37.4	4.825	0.87	NO	0.9

Table 6. Irradiation results of March 1999 experiment on Polyimide Fiberglass.

The above results have the same irradiation parameters with those of runs 7,8,9 of Table 5 except for the higher Pulse Repetition Frequency (PRF) of 37.4 MHz and the longer wavelength λ=4.8 μm. It appears that the shorter wavelength in Table 5 (λ=3.1 μm) combined with the lower PRF is much more effective, resulting in 60% higher penetration depth rate than in table 6. The lower PRF apparently causes more damage, since it results in more energy per pulse for the same average power.

2. Sample #2 - F2 Epoxy

The sample had dimensions 11.5 cm by 10 cm with 1.5 mm thickness, attached to a 1.6 cm thick polyethane foam backing which is clearly seen in Figure 49. In Figure 48, we see a photo of the front of the sample after all sets of irradiations. Irradiations labeled 1, 2 and 3 were those conducted in March 1999. Irradiations 4 to 15 were conducted in August 1999, and 16 to 21 were the last ones conducted in March 2000. Following the same procedure as with polyimide, all the irradiations were done three times with the same parameters in order to get more accurate measurements. The results presented here came from the mean value of the three measurements. Irradiations 7,8,9,10, 11,12,16,17, and 18 (Fig. 48) were done with no airflow while in 4,5,6,13,14,15,19,20,21 there was wind present. In Figure 50, we see a photo of the backside of the sample showing that all of the 10 kW/cm^2 irradiations completely penetrated the sample. On the other hand the 500 W/cm^2 intensity (runs 4 to 9) did not penetrate, but caused more extensive surface damage due to the bigger spot radius.

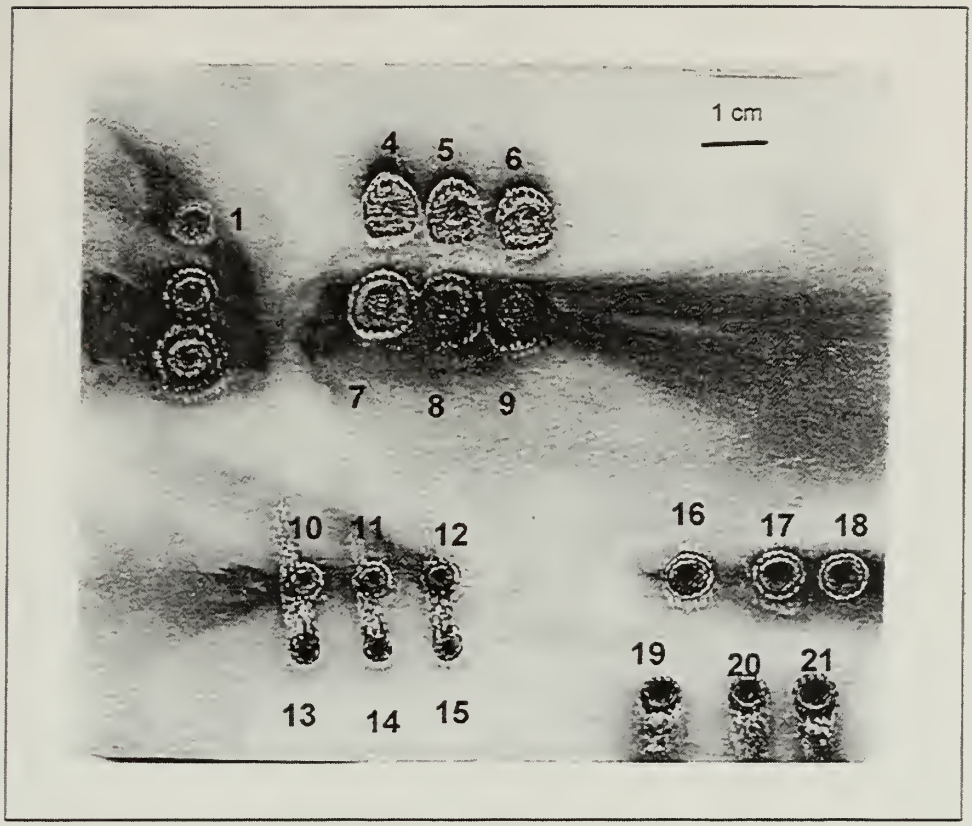

Figure 48. F2 Epoxy (front view).

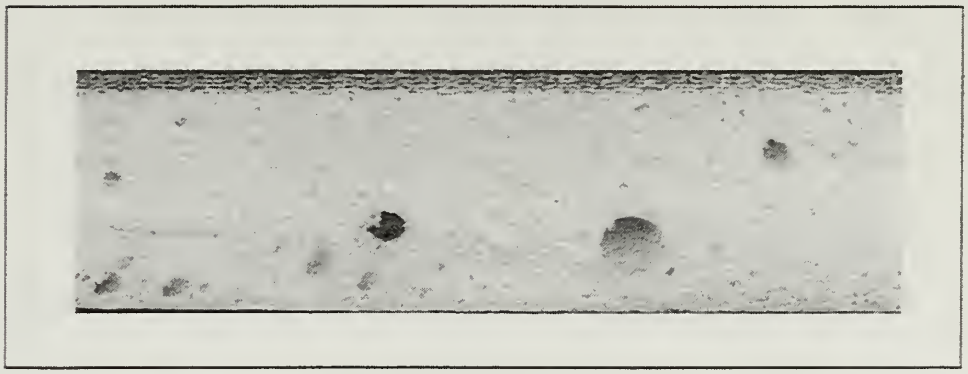

Figure 49. F2 Epoxy (side view).

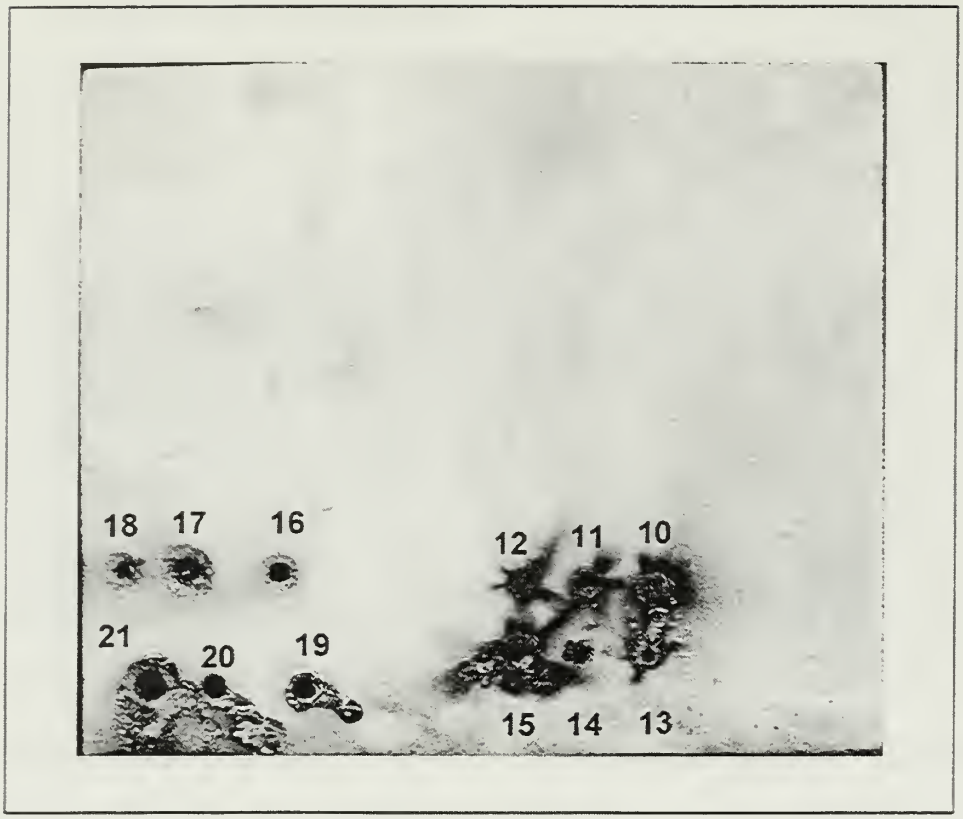

Figure 50. F2 Epoxy (back view).

The presence of the foam layer at the backside of the sample made the measurements of the exit holes diameter unreliable. A closer caption of the damage is presented in Figures 51-56.

Irradiation results are summarized in Table 7. Each row of the table represents a set of three irradiations, conducted with the same characteristics.

Hole Number	Average Power (W)	Average Intensity (kW/cm^2)	PRF (MHz)	λ (μm)	Spot radius (mm)	Wind (mph)	Burn through time (sec)	Penetration Depth Rate (mm/sec)	Front Damage Pattern	Entry Hole Diameter (mm)	Rear Damage Pattern	Exit Hole Diameter (mm)
7,8,9	100	0.5	18.7	3.1	2.5	NO	3.5 *	0.1	Circular	8.7	---	---
4,5,6	100	0.5	18.7	3.1	2.5	60	4 *	0.1	Circular	7.2	---	---
10,11,12	100	10	18.7	3.1	0.87	NO	2.5	0.6	Circular	4.0	Circular	1.2
13,14,15	100	10	18.7	3.1	0.87	60	2.5	0.6	Circular	2.6	Circular	1.1
16,17,18	500	10	37.4	3.1	1.25	NO	1.1	1.4	Slightly elliptical	5.6 x 5.3	circular	2.0
19,20,21	500	10	37.4	3.1	1.25	85	1.0	1.5	Slightly elliptical	5.2 x 4.7	Slightly elliptical	2.2 x 1.8

Table 7. F2 Epoxy irradiations results.

* There was no burn through. The indicated time is the exposure time.

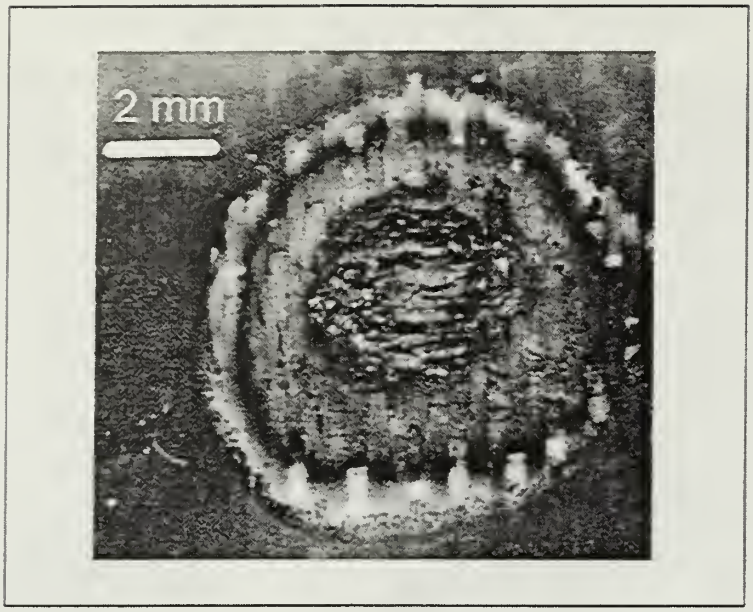

Figure 51. Epoxy, hole 7.
Intensity 500 W / cm^2, no air.
Average Power 100 W. Spot Radius 2.5 mm.

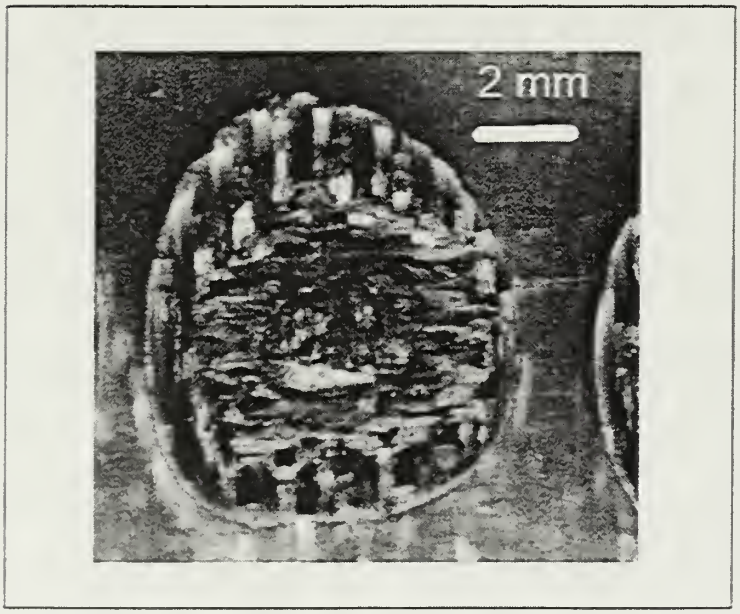

Figure 52. Epoxy, hole 5.
Intensity 500 W / cm^2, with airflow.
Average Power 100 W. Spot Radius 2.5 mm.

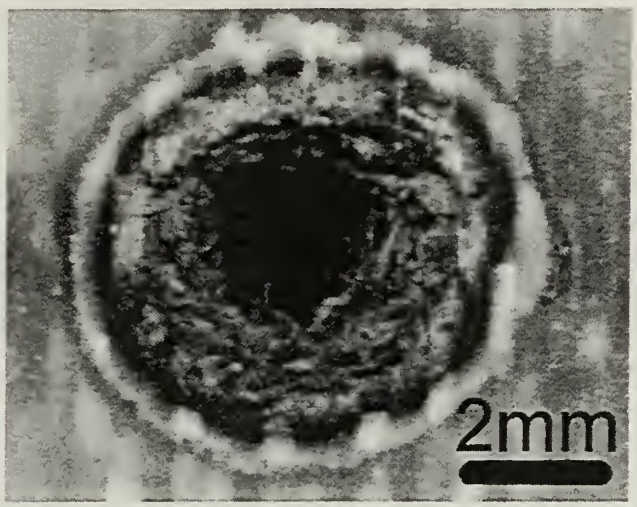

Figure 53. Epoxy, hole 16.
Intensity 10 kW/cm^2, no air.
Average Power 500 W. Spot Radius 1.25 mm.

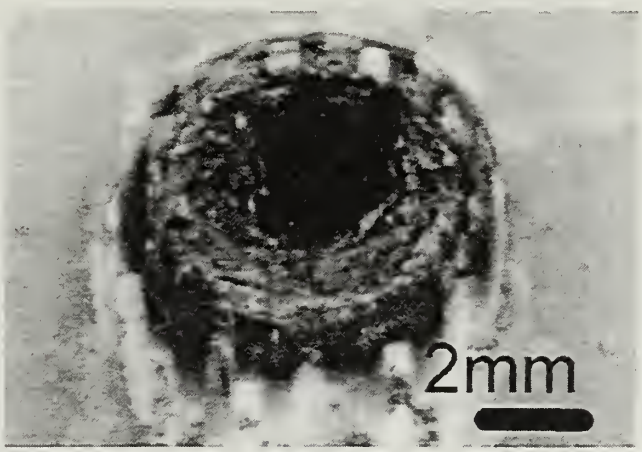

Figure 54. Epoxy, hole 20.
Intensity 10 kW / cm^2, with airflow.
Average Power 500 W. Spot Radius 1.25 mm.

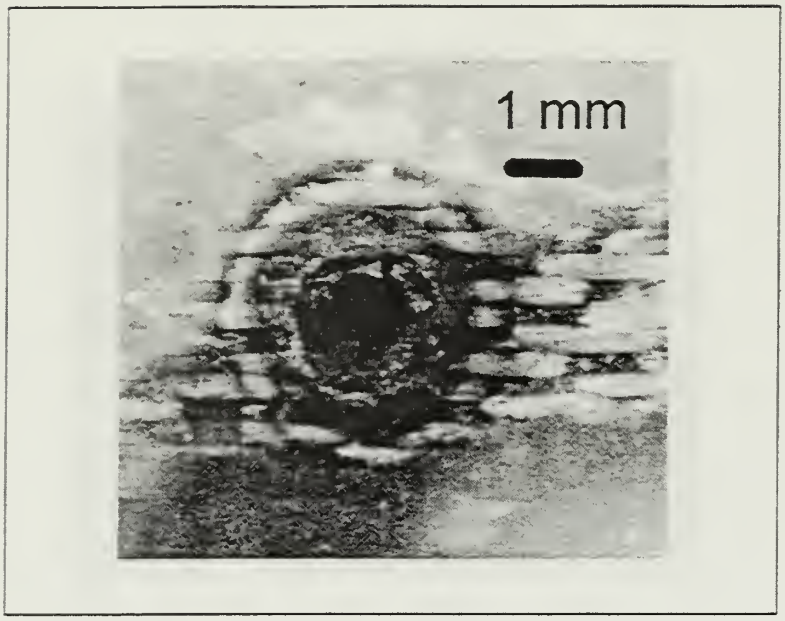

Figure 55. Epoxy, hole 12.
Intensity 10 kW / cm^2, no air.
Average Power 100 W. Spot Radius 0.87 mm.

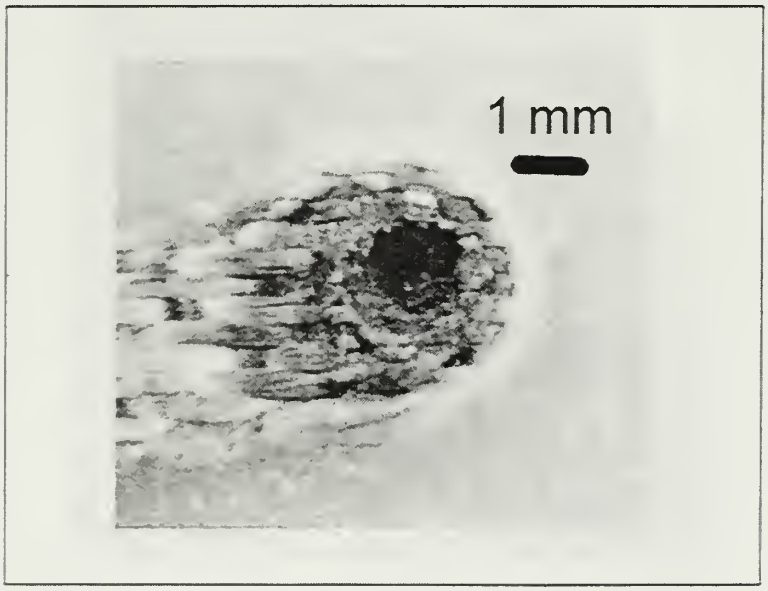

Figure 56. Epoxy, hole 15.
Intensity 10 kW / cm^2, with airflow.
Average Power 100 W. Spot Radius 0.87 mm.

The hole diameters have variation of 15% in each set of three holes. This is again due to the slight variance of the exposure time of the irradiations, which is on the order of 1 to 2 seconds. The presence of airflow did not seem to increase the extent of the damage. The entry hole diameter was actually decreased by 10% to 30%.

The average power of 500 W (runs 16 to 21), resulted in 2.5 times higher penetration rate than the 100 W power (runs 10 to 15), and caused a slightly elliptical damage pattern. During the irradiation, it was observed that flames, smoke, and debris covered the entrance hole. After the irradiation stopped the material was still burning for almost 3 seconds, which caused extra charring and melting of the sample. When airflow was applied, the time decreased by half. The charred region extends approximately 0.5 mm around the entrance hole with wind present and 1 mm without wind. Examination of the holes with a microscope revealed more roughness than the polyimide. This was probably caused by deposited debris and charred material. The Gaussian beam caused the same damage pattern with the polyimide sample, being more intensive at the center of the spot. However the penetration rates were observed to be 2 to 3 times smaller.

Table 8 presents the results of the experiment conducted in March 1999 for the Epoxy sample (Holes 1,2,3).

Average Power (W)	**Average Intensity** (kW/cm^2)	**PRF** (MHz)	**λ** (μm)	**Spot radius** (mm)	**Wind** (mph)	**Penetration Depth Rate** (mm/sec)
100	10	37.4	4.825	0.87	NO	0.1

Table 8. Irradiation results of March 1999 experiment on Epoxy

Comparing these results with runs 10 to 12 of Table 7, it is clear again that the λ=3.1 μm wavelength combined with the lower Pulse Repetition Frequency was more effective, and resulted in 6 times higher penetration depth rate.

E. CONLUSIONS - SUGGESTIONS

When higher laser power is available in the future, the same irradiations should be conducted with even larger spot radii in order to compare the results and establish scaling laws. It is suggested that thicker samples should also be tested in order to determine if the penetration rate stays the same after the laser beam has penetrated the material a few mm.

Airflow did not have a significant effect, possibly because of its relatively low speed. It is suggested that in future experiments the wind speed should be much higher in order to simulate more realistically the conditions of a missile flying with 1 to 2 Mach speed (1000 mph).

Furthermore, a way to make the measurements of burn through times more accurate should be established, as they are important in determining penetration depth rates.

From the analysis of the results, it is apparent that the penetration depth rate is proportional to the laser intensity. When the intensity is changed by a factor of 20 (from 500 W/cm^2 to 10 kW/cm^2) the penetration depth rate is also changed by almost the same factor in both samples.

The λ=3.1 μm wavelength appears to be more effective than the λ=4.875 μm wavelength. In addition, the lower PRF (18.7 MHz) seems to contribute to higher penetration rates due to the higher energy per pulse. It is recommended in future experiments to keep the pulse energy constant, but increase the repetition rate, to see how the burn-through rate is affected. It would be useful also to vary the wavelength, while keeping the PRF and the energy per pulse constant.

THIS PAGE INTENTIONALLY LEFT BLANK

LIST OF REFERENCES

[1] Colson, W.B., Pellegrini, C., *Laser Handbook*, v.6, North-Holland, 1990.

[2] Datoli, G., Renieri, A., and Torre, A., *Lectures on the Free Electron Laser Theory and Related Topics*, World Scientific Publishing Co., 1992.

[3] Colson, W.B., Physics 4055 Course Notes, Naval Postgraduate School, 1999-2000.

[4] Cooper, A.W., and Crittenden, E.C., Physics 4253 Class Notes, Naval Postgraduate School, 1999.

[5] Driggers, R.G., Cox, P. and Edwards, T., Introduction to Infrared and Electro-Optical Systems, chapter 6, Artech House Inc., 1999.

[6] Herbert, P. A., *Anti-ship Missile Defense and the Free Electron Laser, Master's Thesis*, Naval Postgraduate School, Monterey California, December 1998.

[7] Cook, J.R. and Albertine, JR., "High Energy Laser Weapon System," *Surface Warfare*, September/October 1997.

[8] Anderson, E.J., *Total Ship Integration of a Free Electron Laser*, Master's Thesis, Naval Postgraduate School, Monterey California, September 1996.

[9] Wardlaw, N.J., " Defense at the Speed of Light, " *Surface Warfare*, September/October 1997.

[10] Walman, J.P., " The Rolling Airframe Missile," *Surface Warfare*, March/April 1999.

[11] Colson, W.B., Physics 4911 Course Notes, Naval Postgraduate School, 1999-2000.

[12] Ready, J.F., *Industrial Applications of Lasers,* Academic Press, 1978.

[13] Laser Institute of America, Guide for *Material Processing by Lasers,* The Paul M.Harold, 1978.

[14] Thomson, R. W., *Experimental Damage Studies for a Free Electron Laser Weapon, Master's Thesis,* Naval Postgraduate School, Monterey California, June 1999.

[15] Christodoulou, A., Lampiris, D., Colson, W.B., and others, "Simulations of the TJNAF with Tapered and Inversely Tapered Undulators", paper presented at the Free Electron Laser Conference, August 2000.

[16] Benson, S., Gubeli, J., and Neil, G.R., "An Experimental Study of an FEL Oscillator with a Linear Taper", paper presented at the Free Electron Laser Conference, August 2000.

INITIAL DISTRIBUTION LIST

1.	Defense Technical Information Center 8725 John J. Kingman Rd., STE 0944 Ft. Belvoir, VA 22060-6218	2
2.	Dudley Knox Library Naval Postgraduate School 411 Dyer Rd. Monterey, CA 93943-5101	2
3.	Professor William B. Colson, Code PH/Cw Department of Physics Naval Postgraduate School Monterey, CA 93943-5000	2
4.	Professor Robert L. Armstead, Code PH/Ar Department of Physics Naval Postgraduate School Monterey, CA 93943-5000	1
5.	Steve Benson TJNAF 1200 Jefferson Ave. Newport News, VA 23606	1
6.	George Neil TJNAF 1200 Jefferson Ave. Newport News, VA 23606	1
7.	Michelle Shinn TJNAF 1200 Jefferson Ave. Newport News, VA 23606	1
8.	Lieutenant Dimitrios Lampiris 10C Ikarias Rd. Mortero - Nea Erythrea 14671 - Athens Greece	3
9.	Engineering & Technology Curricular Office (Code 34) Naval Postgraduate School Monterey, CA 93943-5000	1